CHAPTER 6

Conclusions

6.1 Summary

This thesis showed results for shock loading of Polymer-Bonded Explosives (PBXs) with varying degrees of microstructural information. Chapter 1 reviewed detonation physics and the composition of PBXs. A review of experimental and numerical work in shock loading of heterogeneous materials showed the need for a multiscale model. Chapter 2 presented the governing equations, models, and numerical methods needed to simulate shock loading of PBXs. The overall solution procedure was presented using the explicit, one-step, second-order Taylor-Galerkin scheme. Chapter 3 thoroughly validated numerical results by comparing them to test problems and experimental PBX results. This chapter used a continuum approach where material properties were constant spatially and microstructural information was incorporated via material constants. Various reaction rate models were studied and showed the effects on run-to-detonation. Mesh density studies were conducted to ensure that the findings were converged and that the shock features were accurately captured. Chapter 4 presented results for Direct Numerical Simulation (DNS) where the microstructure was explicitly modeled. Synthetic microstructures were developed using Markov Random Field approach. Loading conditions for microstructures with varying HMX/binder content were investigated. Average pressure and temperature responses were studied showing the effects of the microstructure on material behavior. Finally, Chapter 5 presented results using First-Order Multiscale modeling. These methods explicitly modeled material heterogeneities in an average sense in a more computationally efficient manner when compared to DNS. The effects of microstructural information on average pressure and temperature responses were studied. Furthermore, results for all methods were compared.

6.2 Concluding Remarks

Various conclusions can be drawn from this work. First, it was shown that material behavior is significantly influenced by information from the microscale. In general, a continuum approach is less reactive than material models that include microscale information. The study of transition from incident pressure shock to steady detonation, shown in Chapter 3, demonstrated that the Arrhenius model alone lacks the micromechanical mechanisms needed to induce prompt reaction. The contrast is shown when comparing to the Ignition and Growth model, where hot spot mechanisms are included in the reaction rate model. Although the Arrhenius model is based on chemistry, they do not follow empirical results for heterogeneous explosives. Furthermore, continuum approach includes binder effects through material properties alone. This inclusion isn't sufficient to fully capture heterogeneous material behavior. These findings are further supported in Chapters 4 and 5, where the continuum is compared to methodologies where the microstructural information is included in other forms. It was observed that the continuum model performed most similarly to higher binder content material systems upon initiation. However, for most loading conditions the continuum model was vastly different than the heterogeneous material systems and never achieved pressure, temperature and burn fractions values similar to those of heterogeneous material systems.

Loading conditions also played a role in material response. Uniform input density and energies produced different responses for various material systems. Therefore, numerical studies compared material systems in an average sense, where pressure and temperature were selected as $P_{avg} \approx 5GPa$ and $T_{avg} \approx 500K$. Four loading conditions were considered, where density and energy were uniformly distributed within regions known as "hot volumes". Under the initial load, it was discovered that loading conditions with similar hot volumes required similar input energy per unit volume required to achieve $P_{avg} = 5GPa$ and $T_{avg} = 500K$. Specifically the pairs $C_1/R_m(12.56\%/10.95\%)$ and $C_2/B_y(7.06\%/6.34\%)$ performed similarly at time $t = 0\,\mu s$. At time $t > 0\,\mu s$ the C_2/B_y pair performed similarly; however, the C_1/R_m pair differed greatly. The R_m loading condition produced significantly higher pressure and temperature values when compared to the other loading conditions. Interestingly, this loading condition had a smaller hot volume than the C_1 loading condition. The differentiating factor is in the way that the hot volumes were distributed. While the C_1 condition was a singular hot spot located at the center of the domain, the R_m loading condition was randomly distributed throughout the domain.

Binder content affects heterogeneous material performance and safety. Material systems with higher binder content required more energy per unit volume to achieve the same average pressures and temperatures reached by other heterogeneous material systems; higher binder content materials are safer. At $t > 0\mu s$, these materials had the lowest performance in terms of pressure and temperature output showing a higher return on energy investment for HMX heavy content materials. This showed the material performance is at competition with material safety. This trend was repeated for all loading conditions. To summarize, HMX heavy materials required less initiation energy and produced the highest temperature and pressure outputs, while binder heavy materials followed the opposite trend. These results have implications for material by design.

Finally, First-Order Multiscale modeling showed the influence of heterogeneity on shock loading of PBXs. The resolution parameter ϕ was introduced and described material heterogeneity or information from the microscale. As the resolution parameter decreased among the multiscale approach, the material became more homogeneous and the response increased. On the other hand increasing the resolution parameter, increased the material heterogeneity and the results were closer to the DNS approach which explicitly models the microstructure. Increasing HMX content among material systems reduced material heterogeneity and yielded pressure and temperature trends that aligned within the multiscale models. Furthermore, these HMX heavy material systems closed the gap between the multiscale approach and DNS. The DNS approach, in general, produced less localized hot spots while the multiscale model produced more. The most hot regions were produced by the homogenized continuum. These localized regions contributed to the overall material response where the DNS approach produced lower pressure and temperature output on average when compared to the multiscale methodologies. Heterogeneous material responses to shock loading can be captured using the multiscale approach at the fraction of the cost associated with DNS.

6.3 Future Work

Several future directions exist to extend the work to a number of topics of interest:

- **Hot Spot Interactions**: Further investigate the R_m loading condition. Specifically find the transition that occurs from the C_1 loading condition to the R_m.
- **Adaptive Mesh Refinement**: High mesh fidelity is not required for the entire domain and high accuracy is only necessary near the shock front. Adaptive meshing schemes can provide a more efficient solution procedure. Though these methods may produce unstructured grids, methods such as domain decomposition may be implemented.

- **Uncertainty quantification in material constants**: Uncertainty quantification of the material response due to variability in microstructure and material constants is useful for understanding the robustness of numerical results and its sensitivity to input parameters [164,165]. Performing this study would allow for the establishment of bounds for material responses.

- **Inclusion of Porosity**: Porosity is also known to have an affect on run-to-detonation of PBXs [48] as pore collapse creates hot spots, the main mechanism for initiation in heterogeneous explosives.

- **Inclusion of metal particles**: PBXs typically have metal particles embedded in a polymeric binder. Adding aluminum content to material greatly influences material behavior [5,6]. Inclusion metal in material models would allow for the study of these effects.

- **Data driven multi–scaling**:Data mining methods may be used to sample from data generated from this thesis. A data driven multiscale model using adaptive sampling from high fidelity micro-scale simulations can be used to mitigate computational expense of concurrent multiscale models [166–168]. At the micro-scale, material responses, or state variables, for multiple microstructures will be determined using DNS. A database will be created for multiple responses of various microstructure, creating a microstructure space. During continuum simulations, material responses will be approximated by adaptively sampling from the microscale calculations, thus reducing the total number of expensive fine-scale calculations which must be performed.

- **Model Improvements**: Include multi-step chemical reaction schemes. Include models for the anisotropic behavior of each HMX crystal. Include temperature dependent heat capacity and thermal conductivity.

- **Inclusion of higher order microstructural features**: Higher order features such as correlation functions carry information about the phase neighborhood in addition to the volume fraction information information [169–171]. Future work should investigate the use of such higher order microstructural information in enhancing the fidelity of multiscaling while still ensuring high computational efficiency.

- **Microstructure design**: Ultimate objective of the numerical approach will be to design optimal microstructures to tailor energy release and sensitivity of the explosives. Future work should investigate optimization techniques that can be used to identify optimal microstructural features that can be used to tailor or modulate the material response at higher length scales [172–175].

Applying the verified methods and techniques used in this dissertation to various PBX systems can allow materials to be designed and tailored to specific applications without having to run physical experiments.

APPENDIX A

Taylor-Galerkin Scheme:1D

Consider a local 1D domain where $i = 1$, $\mathbf{u} = u$ and $\mathbf{x} = x$. Assuming a one-step reaction, the Euler equations (2.18) are

$$\mathbf{U}_t + \boldsymbol{F_1}_x = \mathbf{S} \tag{A.1}$$

where, $(\cdot)_t$ and $(\cdot)_x$ denote partial derivatives in time and space respectively with

$$\mathbf{U} = \begin{bmatrix} \rho \\ \rho u \\ \rho E \\ \rho Y_A \end{bmatrix}, \qquad \boldsymbol{F_1} = \begin{bmatrix} \rho u \\ \rho u^2 + p \\ (\rho E + p)u \\ \rho u Y_A \end{bmatrix}, \qquad and \quad \mathbf{S} = \begin{bmatrix} 0 \\ 0 \\ q\rho \dot{Y}_A \\ \rho \dot{Y}_A \end{bmatrix}. \tag{A.2}$$

The associated weak form, equation 2.35, expressed in 1d is

$$\begin{aligned} \int_x \widetilde{\boldsymbol{U}}^{\boldsymbol{T}} \, \frac{\mathbf{U}^{n+1} - \mathbf{U}^n}{\Delta t} \, dx = \int_x \widetilde{\boldsymbol{U}}^{\boldsymbol{T}}_{\boldsymbol{x}} \, \mathbf{F}^n_{\mathbf{1}} \, dx + \int_x \widetilde{\boldsymbol{U}}^{\boldsymbol{T}} \, \mathbf{S}^n \, dx + \frac{1}{2}\Delta t \int_x \widetilde{\boldsymbol{U}}^{\boldsymbol{T}} \, \mathbf{S}^n_t \, dx \\ + \frac{1}{2}\Delta t \int_x \widetilde{\boldsymbol{U}}^{\boldsymbol{T}}_{\boldsymbol{x}} \, (\mathbf{A}^n_1 \mathbf{S}^n - (\mathbf{A}^n_1)^2 \mathbf{U}^n_x) dx \\ - \left[\widetilde{\boldsymbol{U}}^{\boldsymbol{T}} \, (\mathbf{F}^n_{\mathbf{1}} + \frac{1}{2}\Delta t (\mathbf{F}^n_{\mathbf{1}})_t) \right]_{x=x_1}^{x=x_2} \end{aligned} \tag{A.3}$$

Here, the Jacobian $\mathbf{A}_1$ is given by the following matrix in terms of the pressure gradient $\partial p / \partial \mathbf{U}$

$$\mathbf{A}_1 = \frac{\partial \mathbf{F}_1}{\partial \mathbf{U}} = \begin{bmatrix} 0 & 1 & 0 & 0 \\ -u^2 + \dfrac{\partial p}{\partial \rho} & 2u + \dfrac{\partial p}{\partial \rho u} & \dfrac{\partial p}{\partial \rho E} & \dfrac{\partial p}{\partial \rho Y_A} \\ -uE + u\dfrac{\partial p}{\partial \rho} - u\dfrac{p}{\rho} & E + u\dfrac{\partial p}{\partial \rho u} + \dfrac{p}{\rho} & u + u\dfrac{\partial p}{\partial \rho E} & u\dfrac{\partial p}{\partial \rho Y_A} \\ -uY_A & Y_A & 0 & u \end{bmatrix} \tag{A.4}$$

APPENDIX B

Taylor-Galerkin Scheme:2D

Consider a local 2D domain where $i = 2$, $\mathbf{u} = [u, v]$ and $\mathbf{x} = [x, y]$. Assuming a one-step reaction, the Euler equations (2.18) are

$$\mathbf{U}_t + \boldsymbol{F_1}_x + \boldsymbol{F_2}_y = \mathbf{S} \tag{B.1}$$

where, $(\cdot)_t$ and $(\cdot)_{x,y}$ denote partial derivatives in time and space respectively with

$$\mathbf{U} = \begin{bmatrix} \rho \\ \rho u \\ \rho v \\ \rho E \\ \rho Y_A \end{bmatrix}, \qquad \boldsymbol{F_1} = \begin{bmatrix} \rho u \\ \rho u^2 + p \\ \rho uv \\ (\rho E + p)u \\ \rho u Y_A \end{bmatrix}, \qquad \boldsymbol{F_2} = \begin{bmatrix} \rho v \\ \rho vu \\ \rho v^2 + p \\ (\rho E + p)v \\ \rho v Y_A \end{bmatrix},$$

$$and \quad \mathbf{S} = \begin{bmatrix} 0 \\ 0 \\ 0 \\ q\rho \dot{Y}_A \\ \rho \dot{Y}_A \end{bmatrix} \tag{B.2}$$

The associated weak form, equation 2.35, expressed in 2d is

$$
\begin{aligned}
\int_y \int_x \widetilde{\boldsymbol{U}}^{\boldsymbol{T}} \frac{\mathbf{U}^{n+1} - \mathbf{U}^n}{\Delta t}\, dA = & \int_y \int_x (\widetilde{\boldsymbol{U}}^{\boldsymbol{T}}_{\boldsymbol{x}} \mathbf{F}^n_{\mathbf{1}} + \widetilde{\boldsymbol{U}}^{\boldsymbol{T}}_{\boldsymbol{y}} \mathbf{F}^n_{\mathbf{2}})\, dA \\
& + \int_y \int_x \widetilde{\boldsymbol{U}}^{\boldsymbol{T}} \mathbf{S}^n\, dA + \frac{1}{2}\Delta t \int_y \int_x \widetilde{\boldsymbol{U}}^{\boldsymbol{T}} \mathbf{S}^n_t\, dA \\
& + \frac{1}{2}\Delta t \int_y \int_x \widetilde{\boldsymbol{U}}^{\boldsymbol{T}}_{\boldsymbol{x}} (\mathbf{A}^n_1 \mathbf{S}^n - (\mathbf{A}^n_1)^2 \mathbf{U}^n_x - \mathbf{A}^n_1 \mathbf{A}^n_2 \mathbf{U}^n_y) dA \\
& + \frac{1}{2}\Delta t \int_y \int_x \widetilde{\boldsymbol{U}}^{\boldsymbol{T}}_{\boldsymbol{y}} (\mathbf{A}^n_2 \mathbf{S}^n - \mathbf{A}^n_2 \mathbf{A}^n_1 \mathbf{U}^n_x - (\mathbf{A}^n_2)^2 \mathbf{U}^n_y) dA \\
& - \int_y \left[\widetilde{\boldsymbol{U}}^{\boldsymbol{T}} (\mathbf{F}^n_1 + \frac{1}{2}\Delta t (\mathbf{F}^n_1)_t) \right]^{x_2}_{x_1} dy - \int_x \left[\widetilde{\boldsymbol{U}}^{\boldsymbol{T}} (\mathbf{F}^n_2 + \frac{1}{2}\Delta t (\mathbf{F}^n_2)_t) \right]^{y_2}_{y_1} dx
\end{aligned}
\tag{B.3}
$$

where, $dA = dydx$ and the integration limits are over x and y. Here, the Jacobian's $\mathbf{A}_1$ and $\mathbf{A}_2$ are given by the following matrices in terms of the pressure gradient $\partial p / \partial \mathbf{U}$

$$
\begin{aligned}
\mathbf{A}_1 = & \frac{\partial \mathbf{F}_1}{\partial \mathbf{U}} \\
= & \begin{bmatrix}
0 & 1 & 0 & 0 & 0 \\
-u^2 + \dfrac{\partial p}{\partial \rho} & 2u + \dfrac{\partial p}{\partial \rho u} & \dfrac{\partial p}{\partial \rho v} & \dfrac{\partial p}{\partial \rho E} & \dfrac{\partial p}{\partial \rho Y_A} \\
-uv & v & u & 0 & 0 \\
-uE + u\dfrac{\partial p}{\partial \rho} - u\dfrac{p}{\rho} & E + u\dfrac{\partial p}{\partial \rho u} + \dfrac{p}{\rho} & u\dfrac{\partial p}{\partial \rho v} & u + u\dfrac{\partial p}{\partial \rho E} & u\dfrac{\partial p}{\partial \rho Y_A} \\
-uY_A & Y_A & 0 & 0 & u
\end{bmatrix}
\end{aligned}
\tag{B.4}
$$

$$
\begin{aligned}
\mathbf{A}_2 = & \frac{\partial \mathbf{F}_2}{\partial \mathbf{U}} \\
= & \begin{bmatrix}
0 & 0 & 1 & 0 & 0 \\
-uv & v & u & 0 & 0 \\
-v^2 + \dfrac{\partial p}{\partial \rho} & \dfrac{\partial p}{\partial \rho u} & 2v + \dfrac{\partial p}{\partial \rho v} & \dfrac{\partial p}{\partial \rho E} & \dfrac{\partial p}{\partial \rho Y_A} \\
-vE + v\dfrac{\partial p}{\partial \rho} - v\dfrac{p}{\rho} & v\dfrac{\partial p}{\partial \rho u} & E + v\dfrac{\partial p}{\partial \rho v} + \dfrac{p}{\rho} & v + v\dfrac{\partial p}{\partial \rho E} & v\dfrac{\partial p}{\partial \rho Y_A} \\
-vY_A & 0 & Y_A & 0 & v
\end{bmatrix}
\end{aligned}
\tag{B.5}
$$

APPENDIX C

Taylor-Galerkin Scheme:3D

Consider a local 3D domain where $i = 3$, $\mathbf{u} = [u, v, w]$ and $\mathbf{x} = [x, y, z]$. Assuming a one-step reaction, the Euler equations (2.18) are

$$\mathbf{U}_t + \boldsymbol{F_1}_x + \boldsymbol{F_2}_y + \boldsymbol{F_3}_z = \mathbf{S} \tag{C.1}$$

where, $(\cdot)_t$ and $(\cdot)_{x,y,z}$ denote partial derivatives in time and space respectively with

$$\mathbf{U} = \begin{bmatrix} \rho \\ \rho u \\ \rho v \\ \rho w \\ \rho E \\ \rho Y_A \end{bmatrix}, \quad \boldsymbol{F_1} = \begin{bmatrix} \rho u \\ \rho u^2 + p \\ \rho uv \\ \rho uw \\ (\rho E + p)u \\ \rho u Y_A \end{bmatrix}, \quad \boldsymbol{F_2} = \begin{bmatrix} \rho v \\ \rho vu \\ \rho v^2 + p \\ \rho vw \\ (\rho E + p)v \\ \rho v Y_A \end{bmatrix},$$

$$\boldsymbol{F_3} = \begin{bmatrix} \rho w \\ \rho wu \\ \rho wv \\ \rho w^2 + p \\ (\rho E + p)w \\ \rho w Y_A \end{bmatrix}, \qquad and \quad \mathbf{S} = \begin{bmatrix} 0 \\ 0 \\ 0 \\ 0 \\ q\rho \dot{Y}_A \\ \rho \dot{Y}_A \end{bmatrix} \tag{C.2}$$

The associated weak form, equation 2.35, expressed in 3d is

$$\int_z\int_y\int_x \widetilde{\boldsymbol{U}}^{\boldsymbol{T}}\,\frac{\mathbf{U}^{n+1}-\mathbf{U}^n}{\Delta t}\,dV = \int_z\int_y\int_x(\widetilde{\boldsymbol{U}}_{\boldsymbol{x}}^{\boldsymbol{T}}\,\mathbf{F}_{\mathbf{1}}^n + \widetilde{\boldsymbol{U}}_{\boldsymbol{y}}^{\boldsymbol{T}}\,\mathbf{F}_{\mathbf{2}}^n + \widetilde{\boldsymbol{U}}_{\boldsymbol{z}}^{\boldsymbol{T}}\,\mathbf{F}_{\mathbf{3}}^n)\,dV$$
$$+\int_z\int_y\int_x \widetilde{\boldsymbol{U}}^{\boldsymbol{T}}\,\mathbf{S}^n\,dV + \frac{1}{2}\Delta t\int_z\int_y\int_x \widetilde{\boldsymbol{U}}^{\boldsymbol{T}}\,\mathbf{S}_t^n\,dV$$
$$+\frac{1}{2}\Delta t\int_z\int_y\int_x \widetilde{\boldsymbol{U}}_{\boldsymbol{x}}^{\boldsymbol{T}}(\mathbf{A}_1^n\mathbf{S}^n - (\mathbf{A}_1^n)^2\mathbf{U}_x^n - \mathbf{A}_1^n\mathbf{A}_2^n\mathbf{U}_y^n - \mathbf{A}_1^n\mathbf{A}_3^n\mathbf{U}_z^n)dV$$
$$+\frac{1}{2}\Delta t\int_z\int_y\int_x \widetilde{\boldsymbol{U}}_{\boldsymbol{y}}^{\boldsymbol{T}}(\mathbf{A}_2^n\mathbf{S}^n - \mathbf{A}_2^n\mathbf{A}_1^n\mathbf{U}_x^n - (\mathbf{A}_2^n)^2\mathbf{U}_y^n - \mathbf{A}_2^n\mathbf{A}_3^n\mathbf{U}_z^n)dV$$
$$+\frac{1}{2}\Delta t\int_z\int_y\int_x \widetilde{\boldsymbol{U}}_{\boldsymbol{z}}^{\boldsymbol{T}}(\mathbf{A}_3^n\mathbf{S}^n - \mathbf{A}_3^n\mathbf{A}_1^n\mathbf{U}_x^n - \mathbf{A}_3^n\mathbf{A}_2^n\mathbf{U}_y^n - (\mathbf{A}_3^n)^2\mathbf{U}_3^n)dV$$
$$-\int_z\int_y\left[\widetilde{\boldsymbol{U}}^{\boldsymbol{T}}(\mathbf{F}_1^n + \frac{1}{2}\Delta t(\mathbf{F}_1^n)_t)\right]_{x_1}^{x_2} dydz - \int_z\int_x\left[\widetilde{\boldsymbol{U}}^{\boldsymbol{T}}(\mathbf{F}_2^n + \frac{1}{2}\Delta t(\mathbf{F}_2^n)_t)\right]_{y_1}^{y_2} dxdz$$
$$-\int_y\int_y\left[\widetilde{\boldsymbol{U}}^{\boldsymbol{T}}(\mathbf{F}_3^n + \frac{1}{2}\Delta t(\mathbf{F}_3^n)_t)\right]_{z_1}^{z_2} dxdy \quad \text{(C.3)}$$

where, $dV = dzdydx$ and the integration limits are over x, y and z. Here, the Jacobian's $\mathbf{A}_1$, $\mathbf{A}_2$ and $\mathbf{A}_3$ are given by the following matrices in terms of the pressure gradient $\partial p/\partial\mathbf{U}$

$$A_1 = \frac{\partial F_1}{\partial U} = \quad \text{(C.4)}$$
$$\begin{bmatrix} 0 & 1 & 0 & 0 & 0 & 0 \\ -u^2 + \dfrac{\partial p}{\partial\rho} & 2u + \dfrac{\partial p}{\partial\rho u} & \dfrac{\partial p}{\partial\rho v} & \dfrac{\partial p}{\partial\rho w} & \dfrac{\partial p}{\partial\rho E} & \dfrac{\partial p}{\partial\rho Y_A} \\ -uv & v & u & 0 & 0 & 0 \\ -uw & w & 0 & u & 0 & 0 \\ -uE + u\dfrac{\partial p}{\partial\rho} - u\dfrac{p}{\rho} & E + u\dfrac{\partial p}{\partial\rho u} + \dfrac{p}{\rho} & u\dfrac{\partial p}{\partial\rho v} & u\dfrac{\partial p}{\partial\rho w} & u + u\dfrac{\partial p}{\partial\rho E} & u\dfrac{\partial p}{\partial\rho Y_A} \\ -uY_A & Y_A & 0 & 0 & 0 & u \end{bmatrix}$$

$$A_2 = \frac{\partial F_2}{\partial U} = \tag{C.5}$$

$$\begin{bmatrix} 0 & 0 & 1 & 0 & 0 & 0 \\ -vu & v & u & 0 & 0 & 0 \\ -v^2 + \frac{\partial p}{\partial \rho} & \frac{\partial p}{\partial \rho u} & 2v + \frac{\partial p}{\partial \rho v} & \frac{\partial p}{\partial \rho w} & \frac{\partial p}{\partial \rho E} & \frac{\partial p}{\partial \rho Y_A} \\ -vw & 0 & w & v & 0 & 0 \\ -vE + v\frac{\partial p}{\partial \rho} - v\frac{p}{\rho} & v\frac{\partial p}{\partial \rho u} & E + v\frac{\partial p}{\partial \rho v} + \frac{p}{\rho} & v\frac{\partial p}{\partial \rho w} & v + v\frac{\partial p}{\partial \rho E} & v\frac{\partial p}{\partial \rho Y_A} \\ -vY_A & 0 & Y_A & 0 & 0 & v \end{bmatrix}$$

$$A_3 = \frac{\partial F_3}{\partial U} = \tag{C.6}$$

$$\begin{bmatrix} 0 & 0 & 0 & 1 & 0 & 0 \\ -wu & w & 0 & u & 0 & 0 \\ -wv & 0 & w & v & 0 & 0 \\ -w^2 + \frac{\partial p}{\partial \rho} & \frac{\partial p}{\partial \rho u} & \frac{\partial p}{\partial \rho v} & 2w + \frac{\partial p}{\partial \rho w} & \frac{\partial p}{\partial \rho E} & \frac{\partial p}{\partial \rho Y_A} \\ -wE + w\frac{\partial p}{\partial \rho} - w\frac{p}{\rho} & w\frac{\partial p}{\partial \rho u} & w\frac{\partial p}{\partial \rho v} & E + w\frac{\partial p}{\partial \rho w} + \frac{p}{\rho} & w + w\frac{\partial p}{\partial \rho E} & w\frac{\partial p}{\partial \rho Y_A} \\ -wY_A & 0 & 0 & Y_A & 0 & w \end{bmatrix}$$

APPENDIX D

Equilibrium versus Mixing Rules

In this Section, equilibrium and mixing rules are compared for partially reacted equations of state. For modeling a mixture of solid and gaseous states, it is assumed that the unreacted explosive and reaction products are in temperature and pressure equilibrium; i.e. $T = T_s(\nu_s, e_s) = T_g(\nu_g, e_g)$ and $p = p_s(\nu_s, e_s) = p_g(\nu_g, e_g)$. Equilibrium is enforced by iterating on ν_s and e_s. The following system can be solved using a Newton-Raphson method.

$$\left\{ \begin{array}{c} p_g - p_s \\ T_g - T_s \end{array} \right\} = \left[\begin{array}{cc} \frac{\partial p_s}{\partial \nu_s} - \frac{\partial p_g}{\partial \nu_s} & \frac{\partial p_s}{\partial e_s} - \frac{\partial p_g}{\partial e_s} \\ \frac{\partial T_s}{\partial \nu_s} - \frac{\partial T_g}{\partial \nu_s} & \frac{\partial T_s}{\partial e_s} - \frac{\partial T_g}{\partial e_s} \end{array} \right] \left\{ \begin{array}{c} \delta \nu_s \\ \delta e_s \end{array} \right\} \tag{D.1}$$

To relate the unreacted solid and reaction products, the following mixture rule is used.

$$\nu = (1 - \lambda)\nu_s + \lambda \nu_g \tag{D.2}$$

$$e = (1 - \lambda)e_s + \lambda e_g \tag{D.3}$$

Here, λ is the burn fraction; the mass fraction of detonation products in the mixture. For the one–step reaction in this work, $\lambda = N_B$. Now, the system of equations is closed and both EOS can be expressed in terms of the solid specific volume and internal energy. Mixture rules are shown in equations 2.13 and 2.15 in Chapter 2. The pressure and temperature profiles for PBX 9501 are shown in density-energy space on Figures D.1(a)-D.2(f) and D.3(a)-D.4(f) respectively for each approach. On the y-axis, specific internal energy varies from $e = 0.0 - 0.1\, Mbar cm^3/g$. On the x-axis density varies from $\rho = 1.0 - 3.5\, g/cm^3$. These figures show that there is little difference between these two methods.

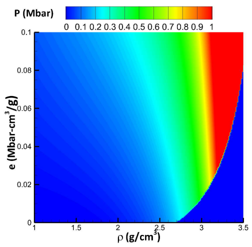

(a) $\lambda = 0.0$

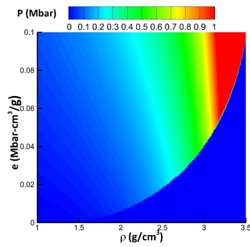

(b) $\lambda = 0.2$

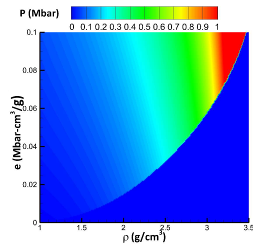

(c) $\lambda = 0.4$

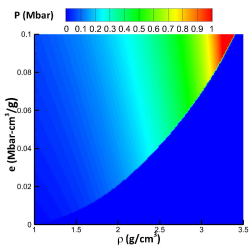

(d) $\lambda = 0.6$

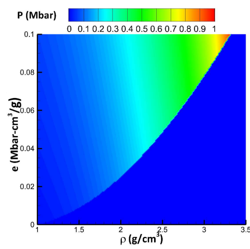

(e) $\lambda = 0.8$

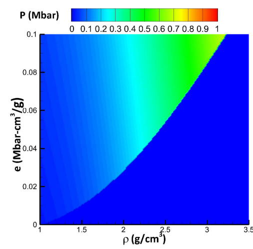

(f) $\lambda = 1.0$

Figure D.1: Pressure profiles using mixture rules for PBX 9501 in density-energy space. Plots vary by $\Delta\lambda = 0.2$.

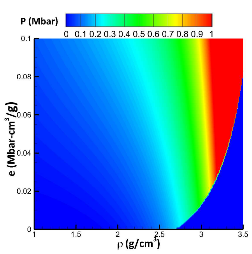

(a) $\lambda = 0.0$

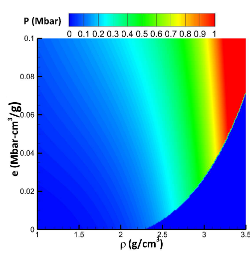

(b) $\lambda = 0.2$

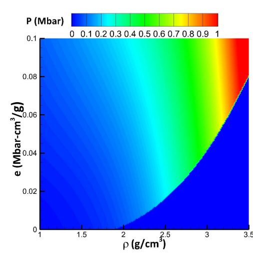

(c) $\lambda = 0.4$

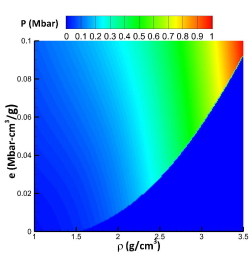

(d) $\lambda = 0.6$

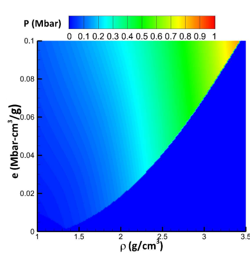

(e) $\lambda = 0.8$

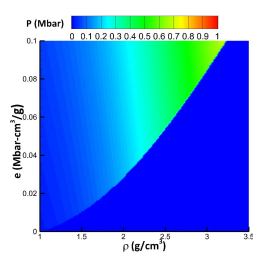

(f) $\lambda = 1.0$

Figure D.2: Pressure profiles using equilibrium for PBX 9501 in density-energy space. Plots vary by $\Delta\lambda = 0.2$.

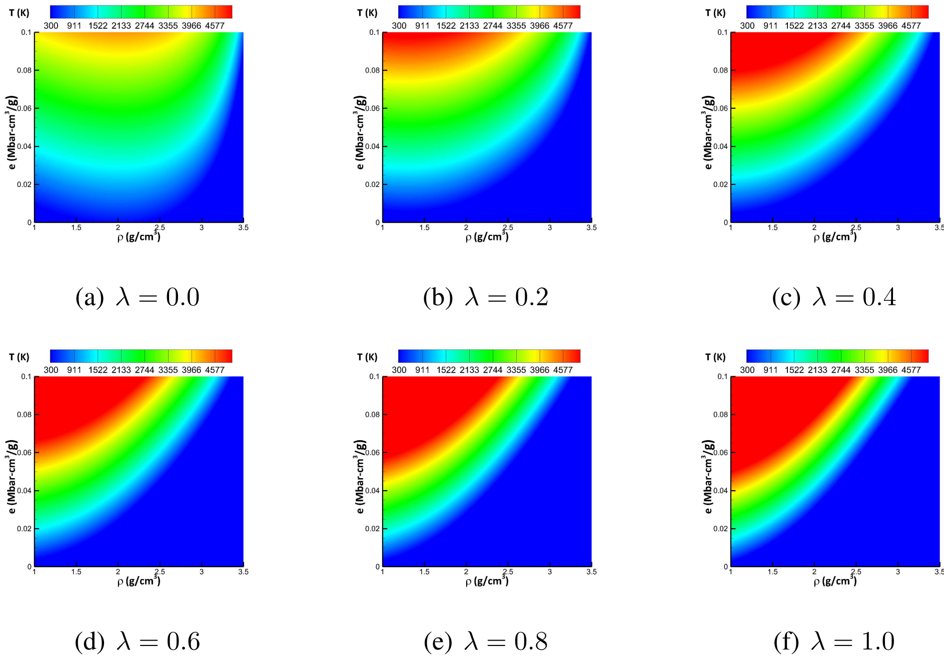

(a) $\lambda = 0.0$ (b) $\lambda = 0.2$ (c) $\lambda = 0.4$

(d) $\lambda = 0.6$ (e) $\lambda = 0.8$ (f) $\lambda = 1.0$

Figure D.3: Temperature profiles using mixture rules for PBX 9501 in density-energy space. Plots vary by $\Delta\lambda = 0.2$.

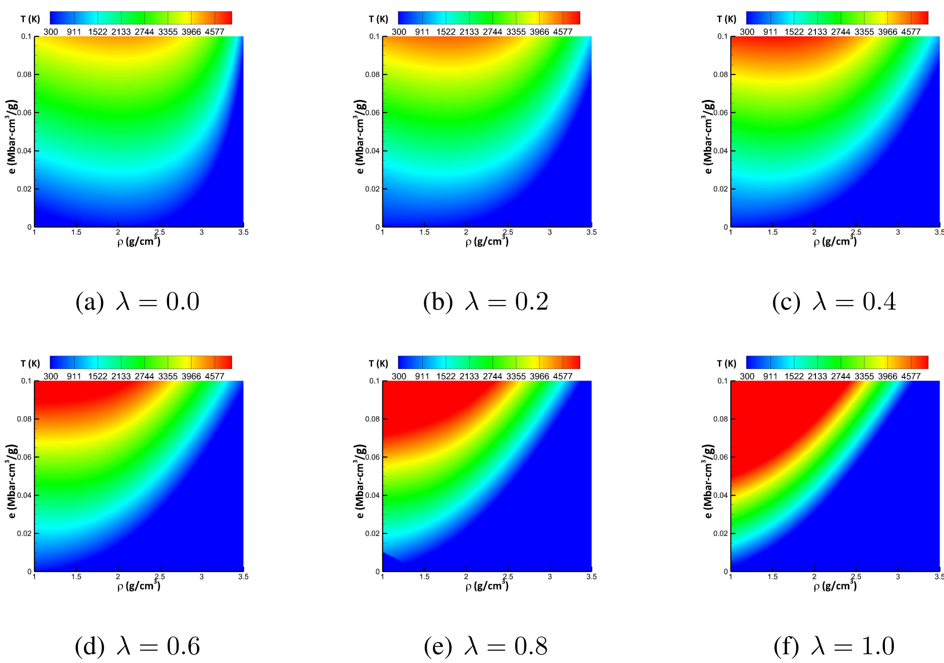

(a) $\lambda = 0.0$ (b) $\lambda = 0.2$ (c) $\lambda = 0.4$

(d) $\lambda = 0.6$ (e) $\lambda = 0.8$ (f) $\lambda = 1.0$

Figure D.4: Temperature profiles using equilibrium for PBX 9501 in density-energy space. Plots vary by $\Delta\lambda = 0.2$.

APPENDIX E

DNS Numerical Results

This Appendix presents Direct Numerical Simulation (DNS) of shock loading of polymer bonded explosives. The results supplement Chapter 4. A uniform mesh, using 3-noded constant strain triangle elements, is considered with a mesh density of $2000ELM/cm$. With 8 local degrees of freedom, and 251001 nodes the global number of degrees of freedom is 2008008. A constant time step of $\Delta t = 1e - 5\mu s$ for a duration of $t = 0.16\mu s$. Computationally, the solution procedure for all results used 8 computational nodes with 16 cores each for a total number of 128 processes.

E.1 Numerical Results: $\eta = 0.75$

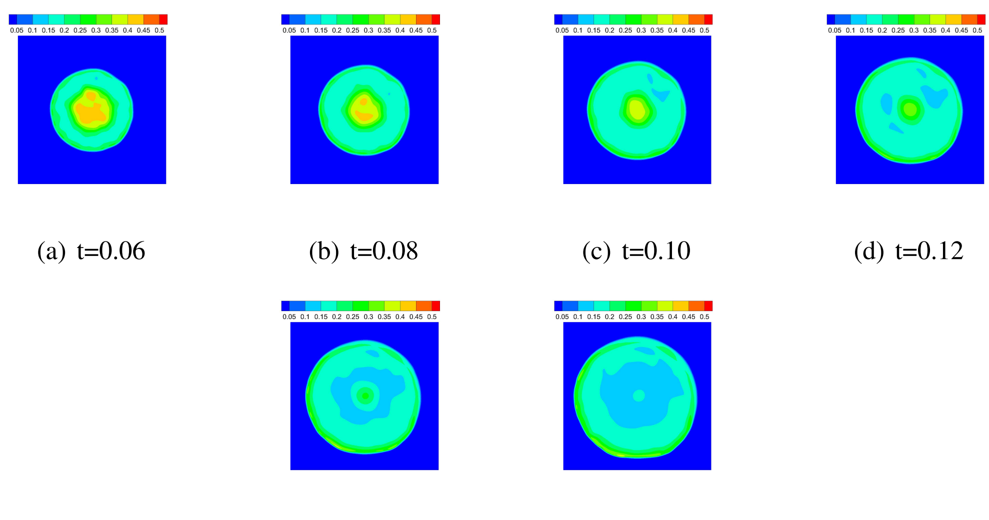

(a) t=0.06 (b) t=0.08 (c) t=0.10 (d) t=0.12

(e) t=0.14 (f) t=0.16

Figure E.1: Pressure contours of $\eta = 0.75$ heterogeneous material under C_1 loading conditions from $t = 0.06 - 0.16\mu s$.

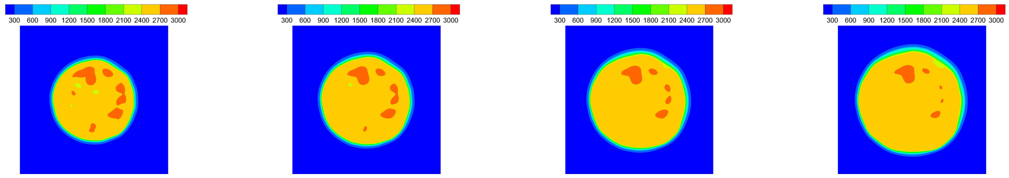

(a) t=0.06 (b) t=0.08 (c) t=0.10 (d) t=0.12

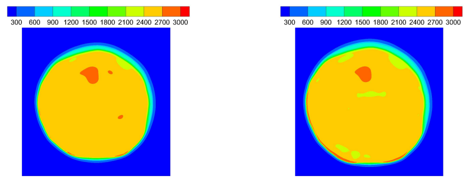

(e) t=0.14 (f) t=0.16

Figure E.2: Temperature contours of $\eta = 0.75$ heterogeneous material under C_1 loading conditions from $t = 0.06 - 0.16\mu s$.

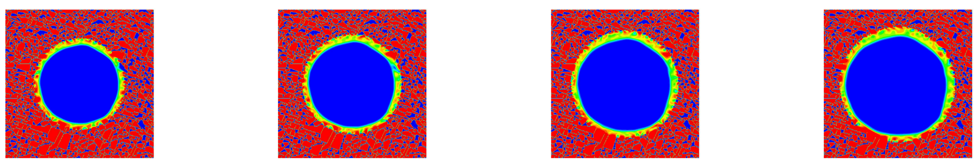

(a) t=0.06 (b) t=0.08 (c) t=0.10 (d) t=0.12

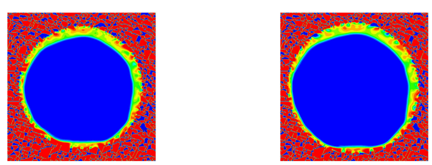

(e) 0.14 (f) 0.16

Figure E.3: HMX fraction contours of $\eta = 0.75$ heterogeneous material under C_1 loading conditions from $t = 0.06 - 0.16\mu s$.

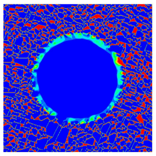

(a) 0.06

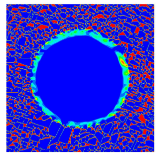

(b) 0.08

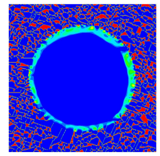

(c) 0.10

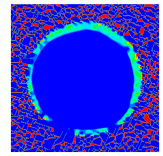

(d) t=0.12

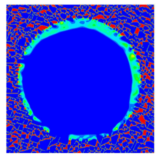

(e) t=0.14

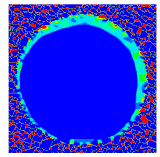

(f) t=0.16

Figure E.4: Solid binder contours of $\eta = 0.75$ heterogeneous material under C_1 loading conditions from $t = 0.06 - 0.16\mu s$.

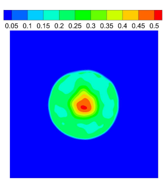

(a) t=0.06

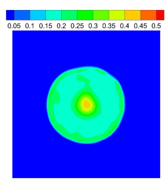

(b) t=0.08

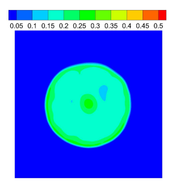

(c) t=0.10

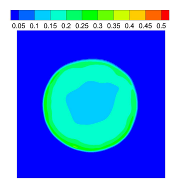

(d) t=0.12

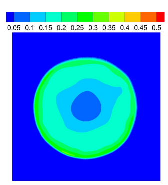

(e) t=0.14

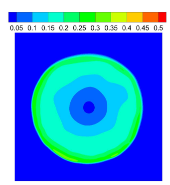

(f) t=0.16

Figure E.5: Pressure contours of $\eta = 0.75$ heterogeneous material under C_2 loading conditions from $t = 0.06 - 0.16\mu s$.

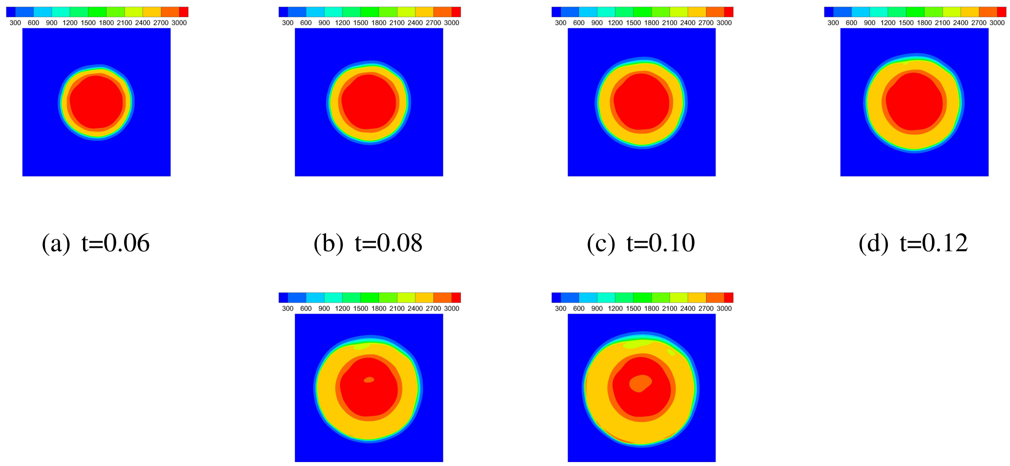

(a) t=0.06 (b) t=0.08 (c) t=0.10 (d) t=0.12

(e) t=0.14 (f) t=0.16

Figure E.6: Temperature contours of $\eta = 0.75$ heterogeneous material under C_2 loading conditions from $t = 0.06 - 0.16\mu s$.

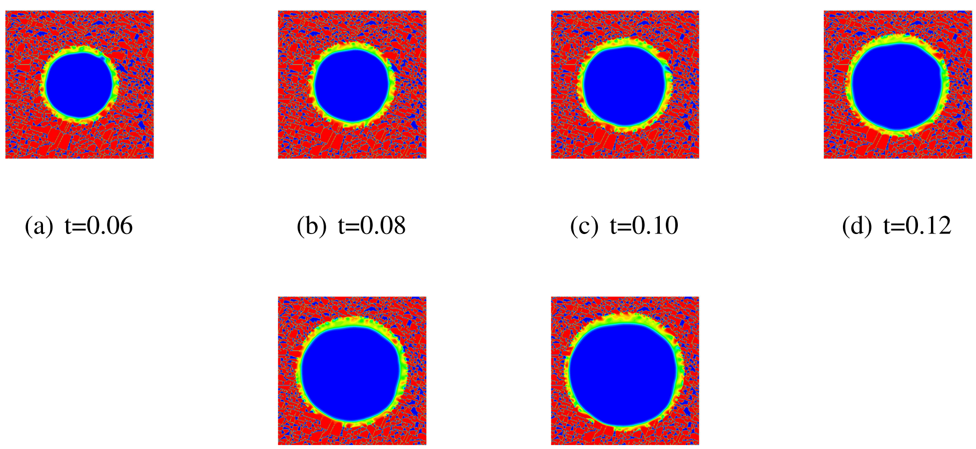

(a) t=0.06 (b) t=0.08 (c) t=0.10 (d) t=0.12

(e) 0.14 (f) 0.16

Figure E.7: HMX fraction contours of $\eta = 0.75$ heterogeneous material under C_2 loading conditions from $t = 0.06 - 0.16\mu s$.

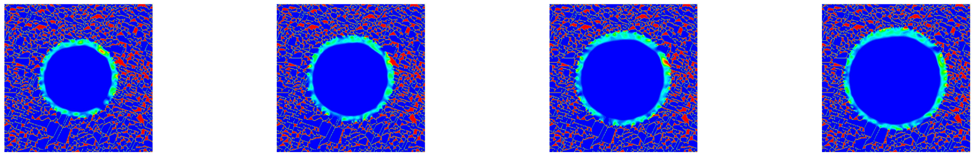

(a) 0.06 (b) 0.08 (c) 0.10 (d) t=0.12

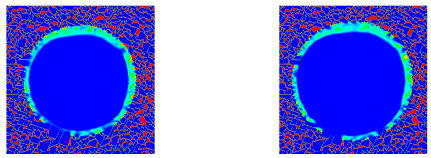

(e) t=0.14 (f) t=0.16

Figure E.8: Solid binder contours of $\eta = 0.75$ heterogeneous material under C_2 loading conditions from $t = 0.06 - 0.16\mu s$.

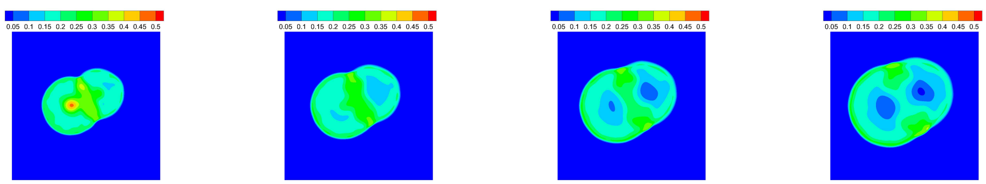

(a) t=0.06 (b) t=0.08 (c) t=0.10 (d) t=0.12

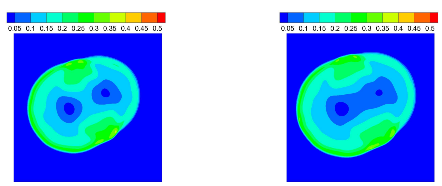

(e) t=0.14 (f) t=0.16

Figure E.9: Pressure contours of $\eta = 0.75$ heterogeneous material under B_Y loading conditions from $t = 0.06 - 0.16\mu s$.

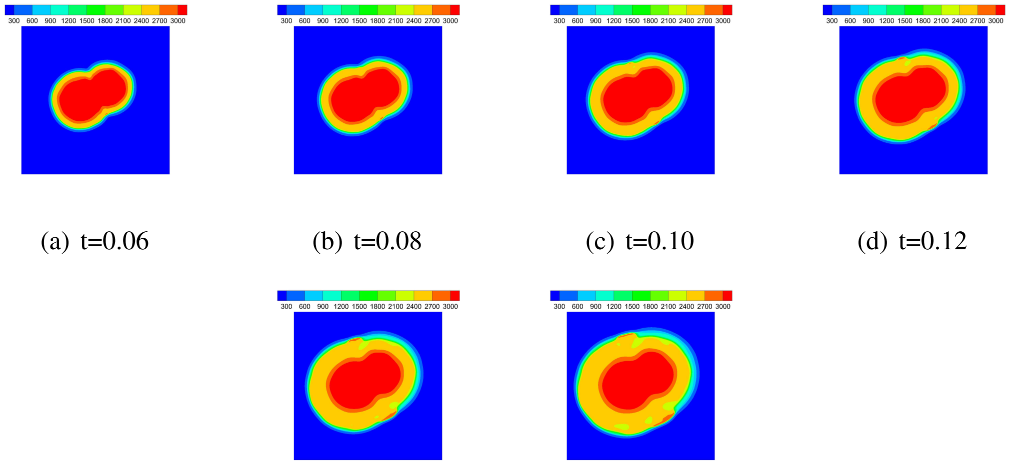

(a) t=0.06 (b) t=0.08 (c) t=0.10 (d) t=0.12

(e) t=0.14 (f) t=0.16

Figure E.10: Temperature contours of $\eta = 0.75$ heterogeneous material under B_Y loading conditions from $t = 0.06 - 0.16\mu s$.

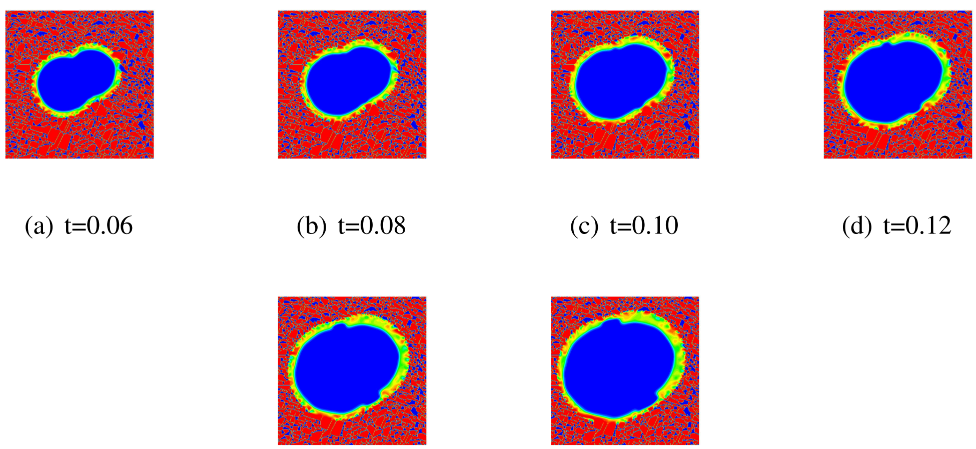

(a) t=0.06 (b) t=0.08 (c) t=0.10 (d) t=0.12

(e) 0.14 (f) 0.16

Figure E.11: HMX fraction contours of $\eta = 0.75$ heterogeneous material under B_Y loading conditions from $t = 0.06 - 0.16\mu s$.

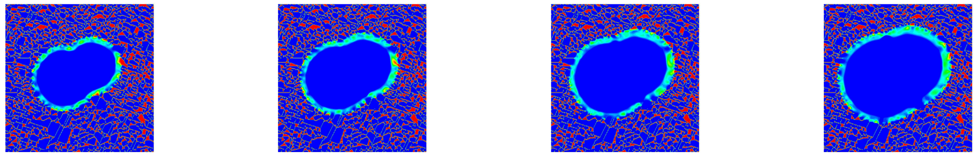

(a) 0.06 (b) 0.08 (c) 0.10 (d) t=0.12

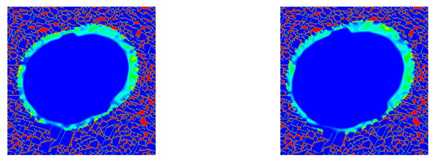

(e) t=0.14 (f) t=0.16

Figure E.12: Solid binder contours of $\eta = 0.75$ heterogeneous material under B_Y loading conditions from $t = 0.06 - 0.16\mu s$.

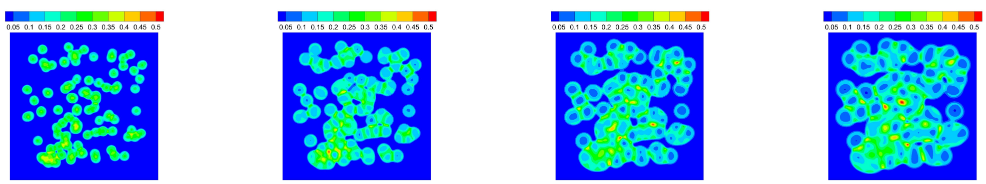

(a) t=0.01 (b) t=0.02 (c) t=0.03 (d) t=0.04

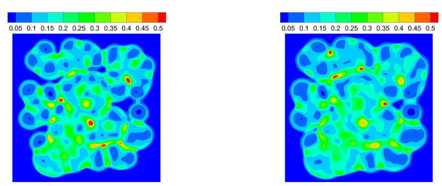

(e) t=0.05 (f) t=0.06

Figure E.13: Pressure contours of $\eta = 0.75$ heterogeneous material under B_Y loading conditions from $t = 0.06 - 0.16\mu s$.

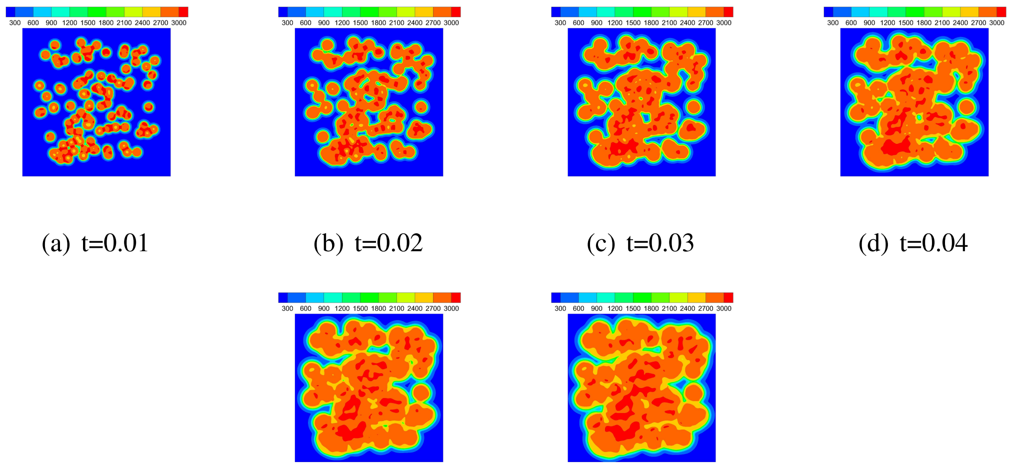

(a) t=0.01 (b) t=0.02 (c) t=0.03 (d) t=0.04

(e) t=0.05 (f) t=0.06

Figure E.14: Temperature contours of $\eta = 0.75$ heterogeneous material under B_Y loading conditions from $t = 0.06 - 0.16\mu s$.

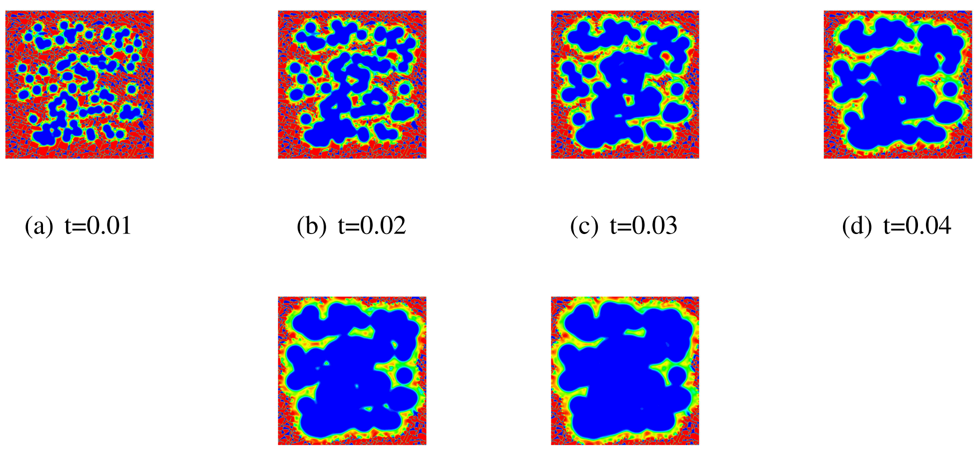

(a) t=0.01 (b) t=0.02 (c) t=0.03 (d) t=0.04

(e) t=0.05 (f) t=0.06

Figure E.15: HMX contours of $\eta = 0.75$ heterogeneous material under B_Y loading conditions from $t = 0.06 - 0.16\mu s$.

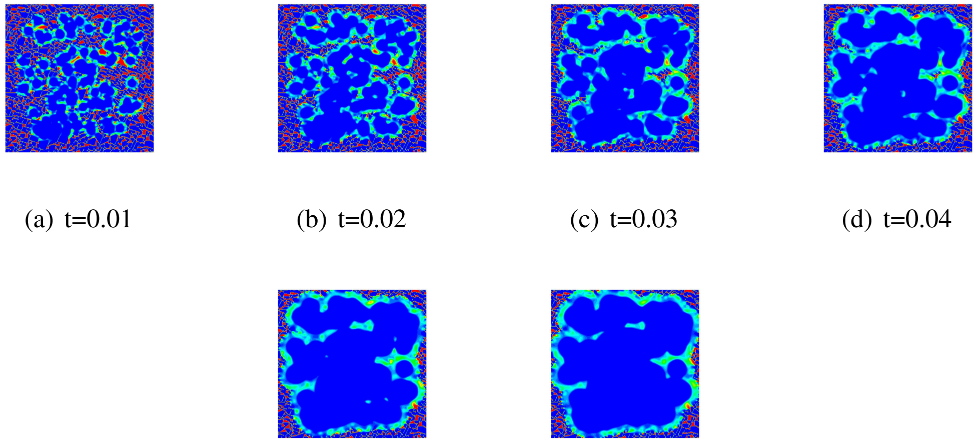

(a) t=0.01 (b) t=0.02 (c) t=0.03 (d) t=0.04

(e) t=0.05 (f) t=0.06

Figure E.16: Binder contours of $\eta = 0.75$ heterogeneous material under R_m loading conditions from $t = 0.06 - 0.16\mu s$.

E.2 Numerical Results: $\eta = 0.85$

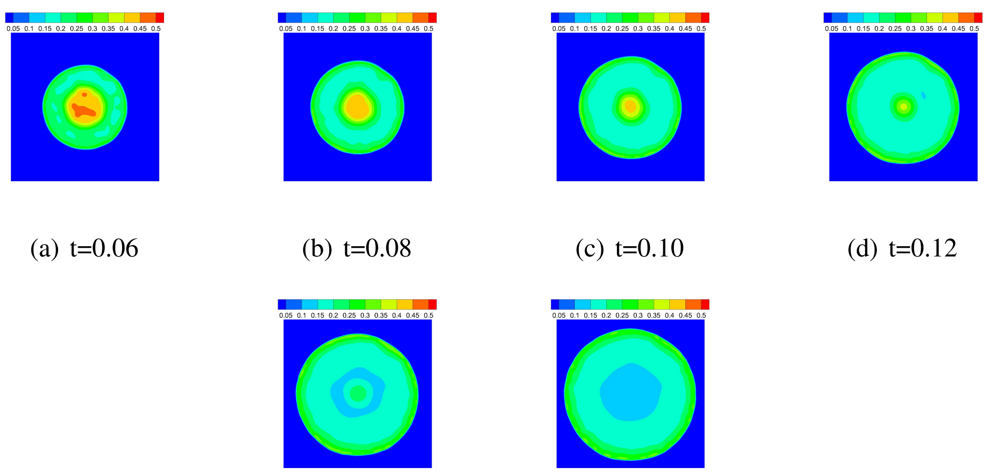

(a) t=0.06 (b) t=0.08 (c) t=0.10 (d) t=0.12

(e) t=0.14 (f) t=0.16

Figure E.17: Pressure contours of $\eta = 0.85$ heterogeneous material under C_1 loading conditions from $t = 0.06 - 0.16\mu s$.

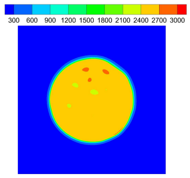

(a) t=0.06

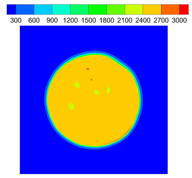

(b) t=0.08

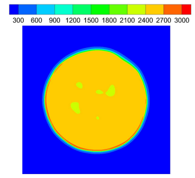

(c) t=0.10

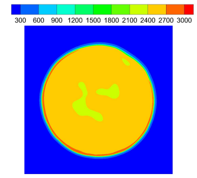

(d) t=0.12

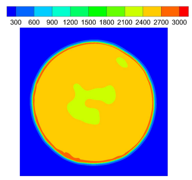

(e) t=0.14

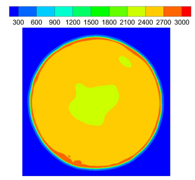

(f) t=0.16

Figure E.18: Temperature contours of $\eta = 0.85$ heterogeneous material under C_1 loading conditions from $t = 0.06 - 0.16\mu s$.

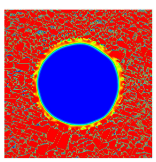

(a) t=0.06

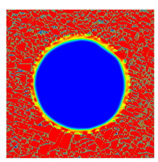

(b) t=0.08

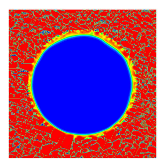

(c) t=0.10

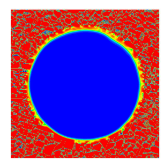

(d) t=0.12

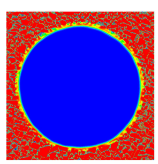

(e) 0.14

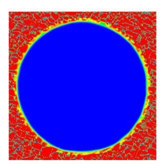

(f) 0.16

Figure E.19: HMX fraction contours of $\eta = 0.85$ heterogeneous material under C_1 loading conditions from $t = 0.06 - 0.16\mu s$.

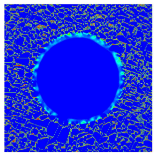

(a) 0.06

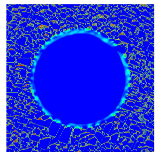

(b) 0.08

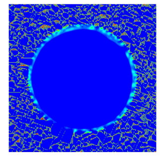

(c) 0.10

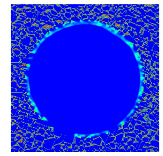

(d) t=0.12

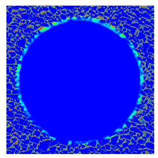

(e) t=0.14

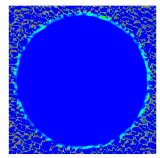

(f) t=0.16

Figure E.20: Solid binder contours of $\eta = 0.85$ heterogeneous material under C_1 loading conditions from $t = 0.06 - 0.16\mu s$.

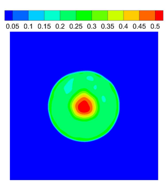

(a) t=0.06

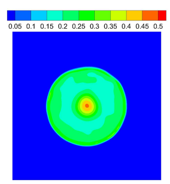

(b) t=0.08

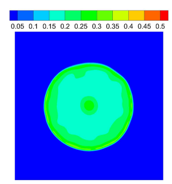

(c) t=0.10

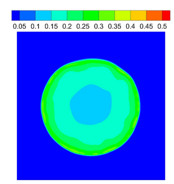

(d) t=0.12

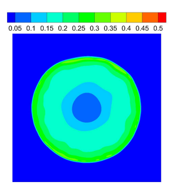

(e) t=0.14

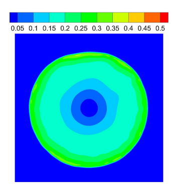

(f) t=0.16

Figure E.21: Pressure contours of $\eta = 0.85$ heterogeneous material under C_2 loading conditions from $t = 0.06 - 0.16\mu s$.

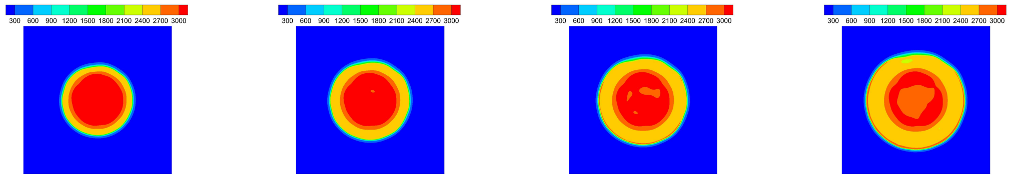

(a) t=0.06 (b) t=0.08 (c) t=0.10 (d) t=0.12

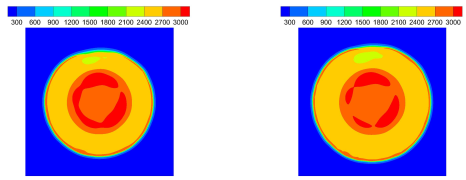

(e) t=0.14 (f) t=0.16

Figure E.22: Temperature contours of $\eta = 0.85$ heterogeneous material under C_2 loading conditions from $t = 0.06 - 0.16\mu s$.

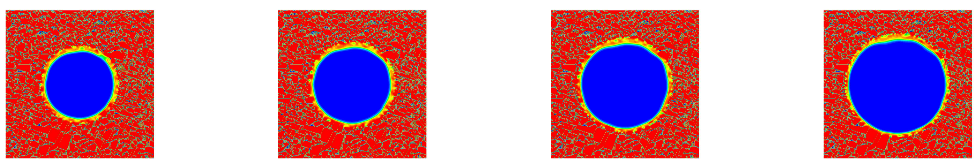

(a) t=0.06 (b) t=0.08 (c) t=0.10 (d) t=0.12

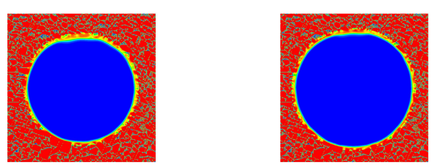

(e) 0.14 (f) 0.16

Figure E.23: HMX fraction contours of $\eta = 0.85$ heterogeneous material under C_2 loading conditions from $t = 0.06 - 0.16\mu s$.

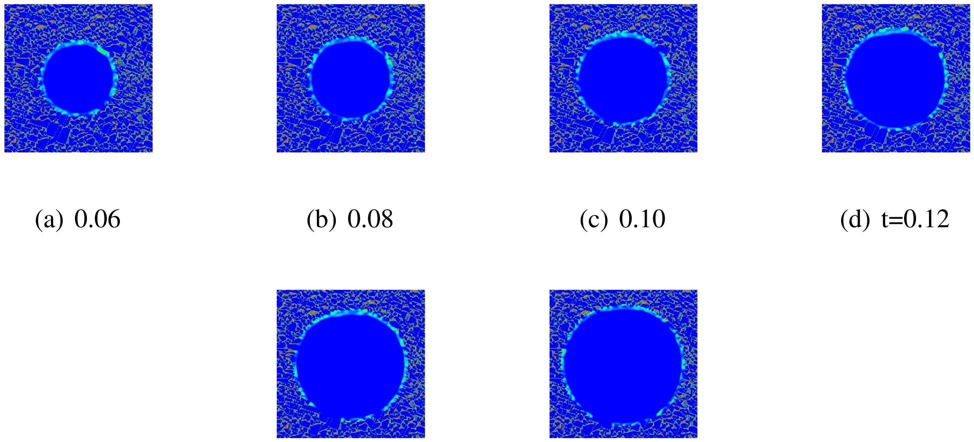

(a) 0.06 (b) 0.08 (c) 0.10 (d) t=0.12

(e) t=0.14 (f) t=0.16

Figure E.24: Solid binder contours of $\eta = 0.85$ heterogeneous material under C_2 loading conditions from $t = 0.06 - 0.16\mu s$.

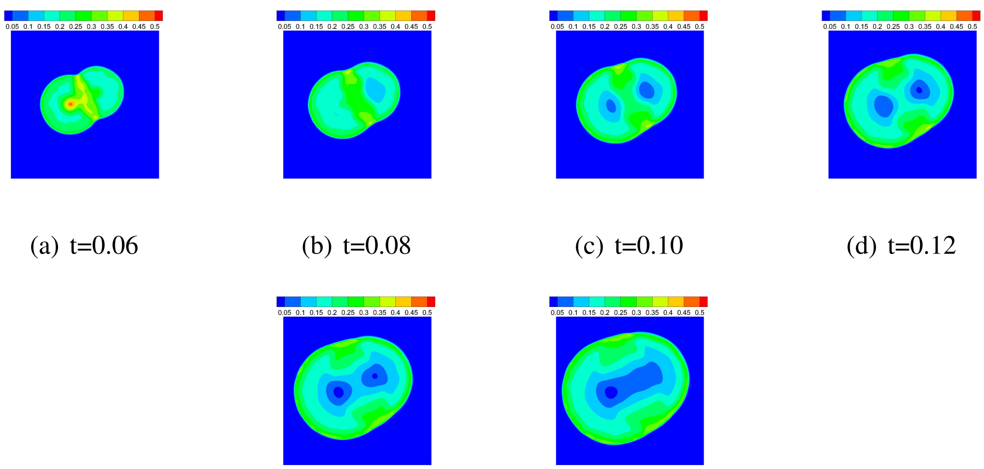

(a) t=0.06 (b) t=0.08 (c) t=0.10 (d) t=0.12

(e) t=0.14 (f) t=0.16

Figure E.25: Pressure contours of $\eta = 0.85$ heterogeneous material under B_Y loading conditions from $t = 0.06 - 0.16\mu s$.

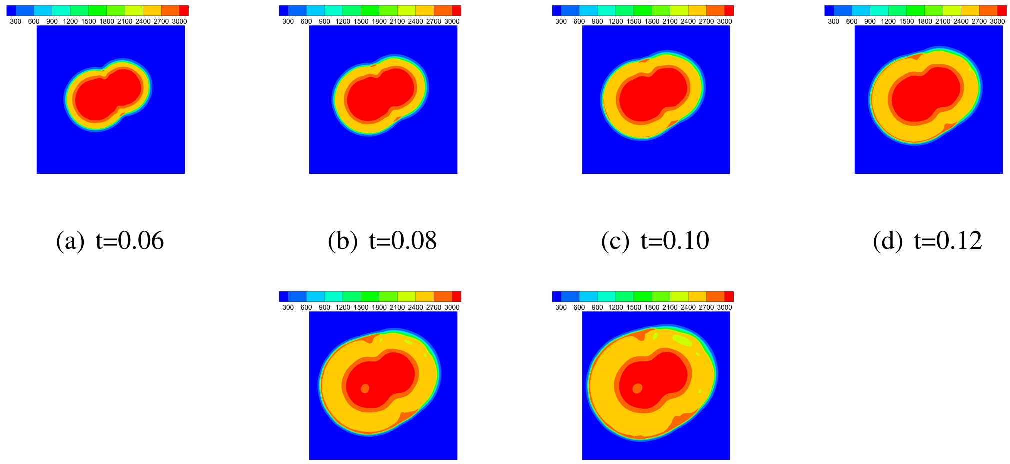

(a) t=0.06 (b) t=0.08 (c) t=0.10 (d) t=0.12

(e) t=0.14 (f) t=0.16

Figure E.26: Temperature contours of $\eta = 0.85$ heterogeneous material under B_Y loading conditions from $t = 0.06 - 0.16\mu s$.

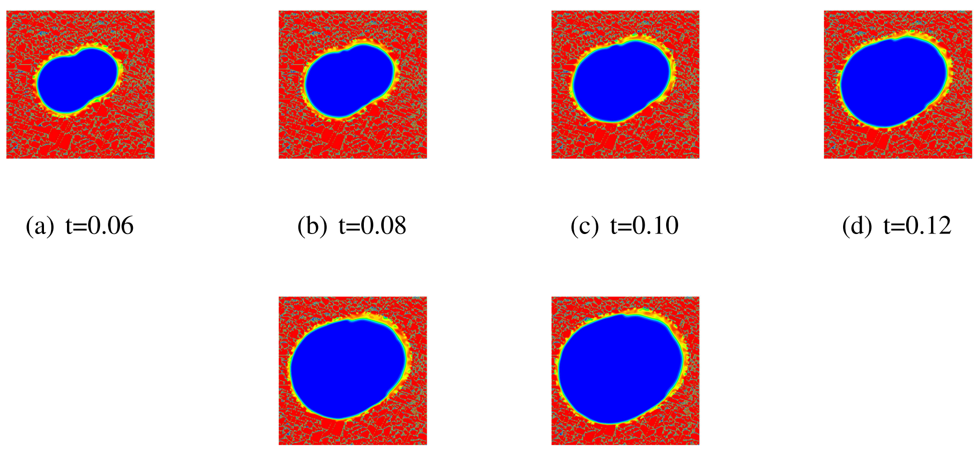

(a) t=0.06 (b) t=0.08 (c) t=0.10 (d) t=0.12

(e) 0.14 (f) 0.16

Figure E.27: HMX fraction contours of $\eta = 0.85$ heterogeneous material under B_Y loading conditions from $t = 0.06 - 0.16\mu s$.

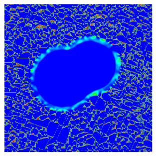

(a) 0.06

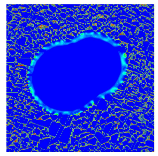

(b) 0.08

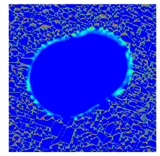

(c) 0.10

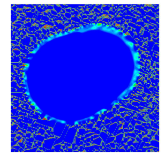

(d) t=0.12

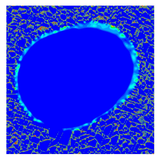

(e) t=0.14

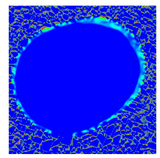

(f) t=0.16

Figure E.28: Solid binder contours of $\eta = 0.85$ heterogeneous material under B_Y loading conditions from $t = 0.06 - 0.16\mu s$.

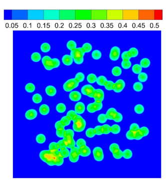

(a) t=0.01

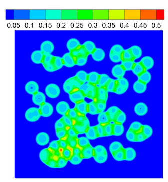

(b) t=0.02

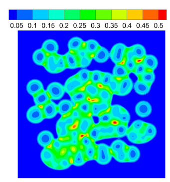

(c) t=0.03

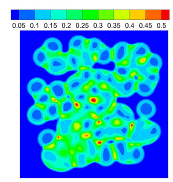

(d) t=0.04

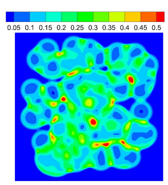

(e) t=0.05

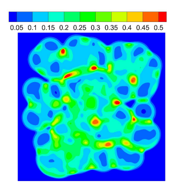

(f) t=0.06

Figure E.29: Pressure contours of $\eta = 0.85$ heterogeneous material under B_Y loading conditions from $t = 0.06 - 0.16\mu s$.

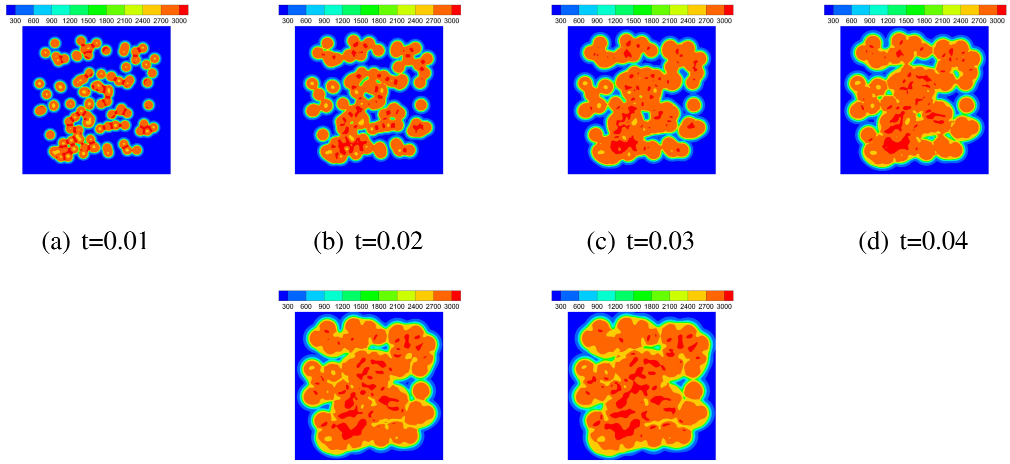

(a) t=0.01 (b) t=0.02 (c) t=0.03 (d) t=0.04

(e) t=0.05 (f) t=0.06

Figure E.30: Temperature contours of $\eta = 0.85$ heterogeneous material under B_Y loading conditions from $t = 0.06 - 0.16\mu s$.

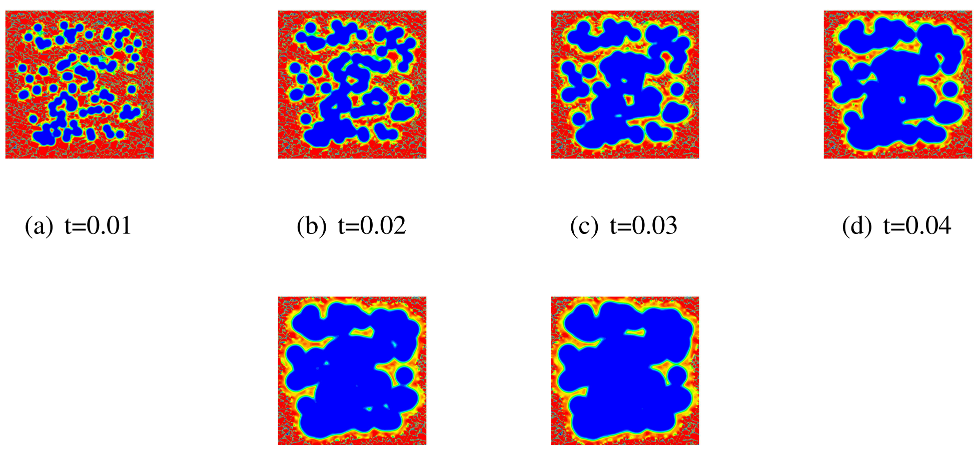

(a) t=0.01 (b) t=0.02 (c) t=0.03 (d) t=0.04

(e) t=0.05 (f) t=0.06

Figure E.31: HMX contours of $\eta = 0.85$ heterogeneous material under B_Y loading conditions from $t = 0.06 - 0.16\mu s$.

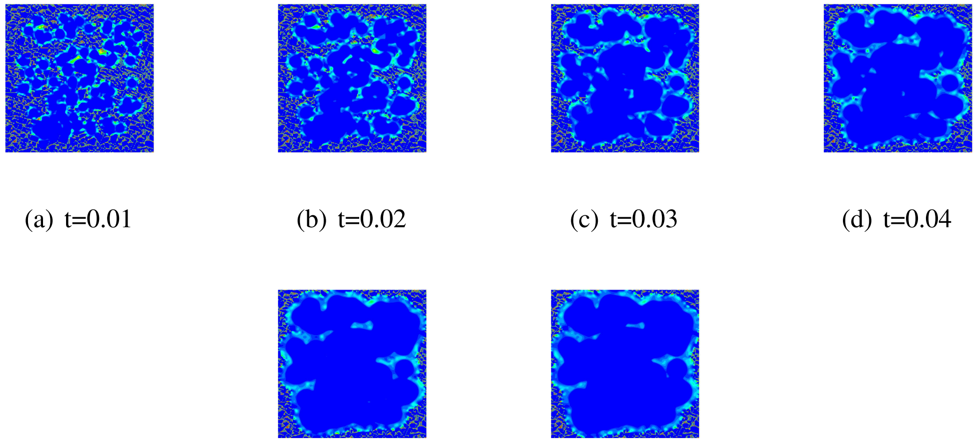

(a) t=0.01 (b) t=0.02 (c) t=0.03 (d) t=0.04

(e) t=0.05 (f) t=0.06

Figure E.32: Binder contours of $\eta = 0.85$ heterogeneous material under R_m loading conditions from $t = 0.06 - 0.16\mu s$.

E.3 Numerical Results: $\eta = 0.95$

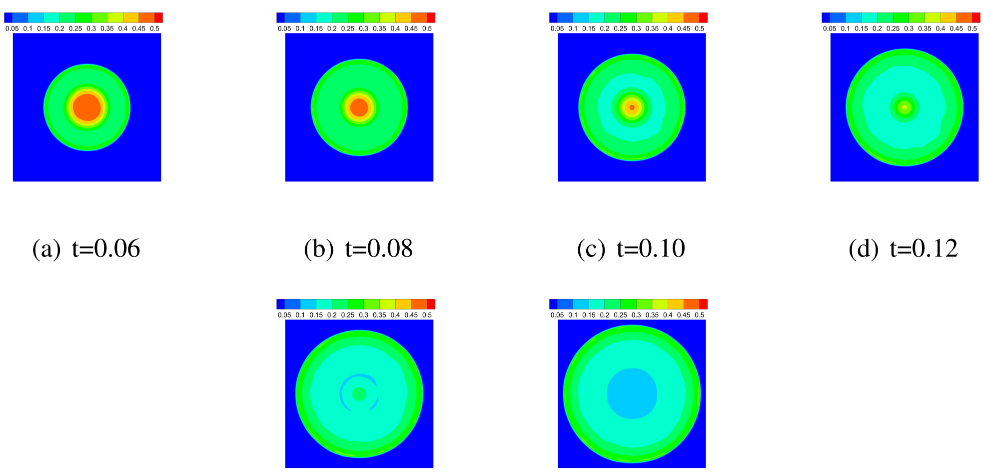

(a) t=0.06 (b) t=0.08 (c) t=0.10 (d) t=0.12

(e) t=0.14 (f) t=0.16

Figure E.33: Pressure contours of $\eta = 0.95$ heterogeneous material under C_1 loading conditions from $t = 0.06 - 0.16\mu s$.

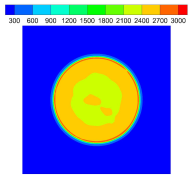

(a) t=0.06

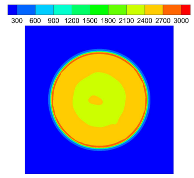

(b) t=0.08

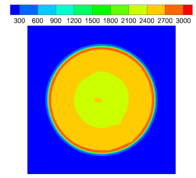

(c) t=0.10

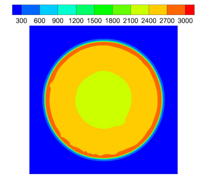

(d) t=0.12

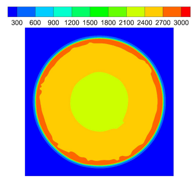

(e) t=0.14

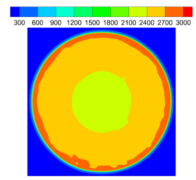

(f) t=0.16

Figure E.34: Temperature contours of $\eta = 0.95$ heterogeneous material under C_1 loading conditions from $t = 0.06 - 0.16\mu s$.

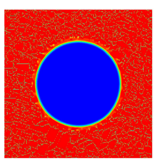

(a) t=0.06

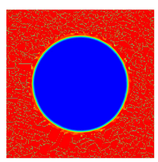

(b) t=0.08

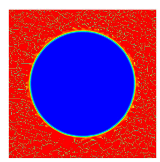

(c) t=0.10

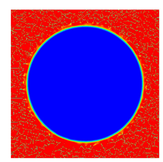

(d) t=0.12

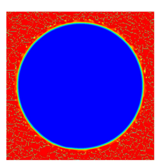

(e) 0.14

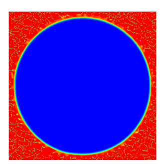

(f) 0.16

Figure E.35: HMX fraction contours of $\eta = 0.95$ heterogeneous material under C_1 loading conditions from $t = 0.06 - 0.16\mu s$.

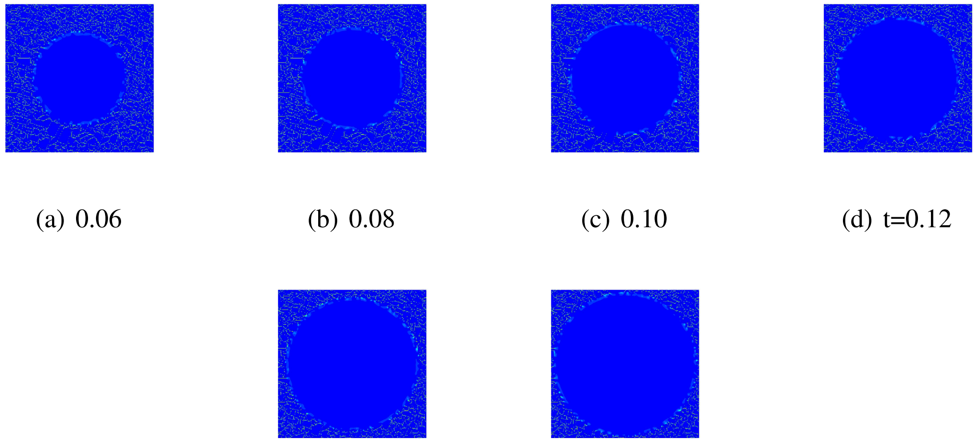

(a) 0.06 (b) 0.08 (c) 0.10 (d) t=0.12

(e) t=0.14 (f) t=0.16

Figure E.36: Solid binder contours of $\eta = 0.95$ heterogeneous material under C_1 loading conditions from $t = 0.06 - 0.16 \mu s$.

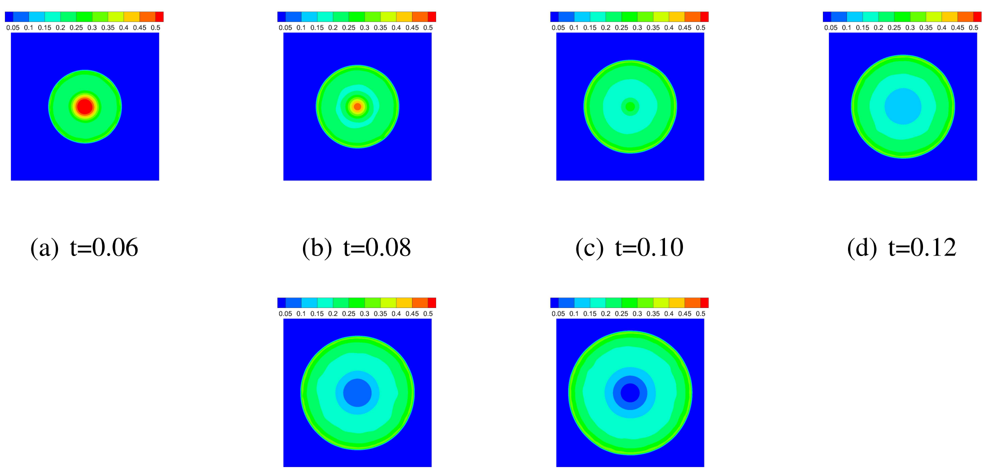

(a) t=0.06 (b) t=0.08 (c) t=0.10 (d) t=0.12

(e) t=0.14 (f) t=0.16

Figure E.37: Pressure contours of $\eta = 0.95$ heterogeneous material under C_2 loading conditions from $t = 0.06 - 0.16 \mu s$.

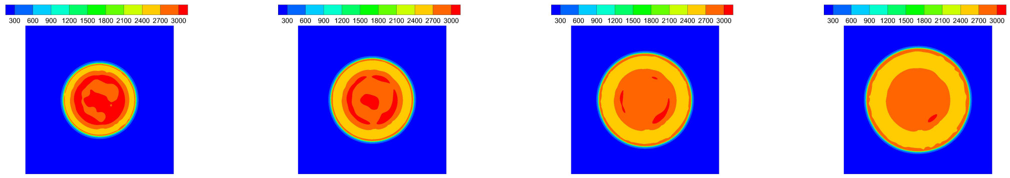

(a) t=0.06 (b) t=0.08 (c) t=0.10 (d) t=0.12

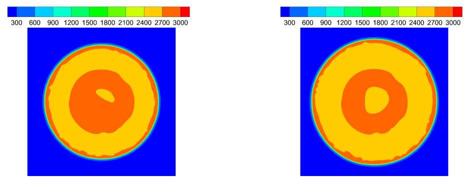

(e) t=0.14 (f) t=0.16

Figure E.38: Temperature contours of $\eta = 0.95$ heterogeneous material under C_2 loading conditions from $t = 0.06 - 0.16\mu s$.

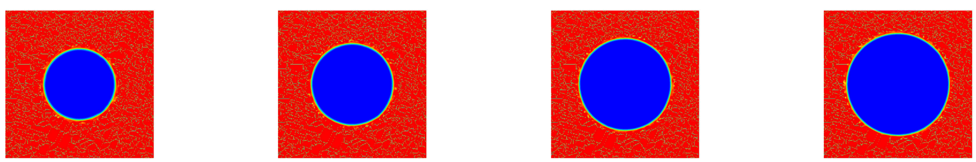

(a) t=0.06 (b) t=0.08 (c) t=0.10 (d) t=0.12

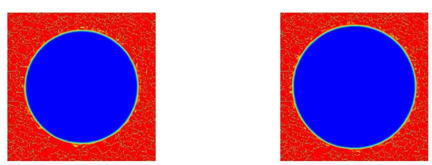

(e) 0.14 (f) 0.16

Figure E.39: HMX fraction contours of $\eta = 0.95$ heterogeneous material under C_2 loading conditions from $t = 0.06 - 0.16\mu s$.

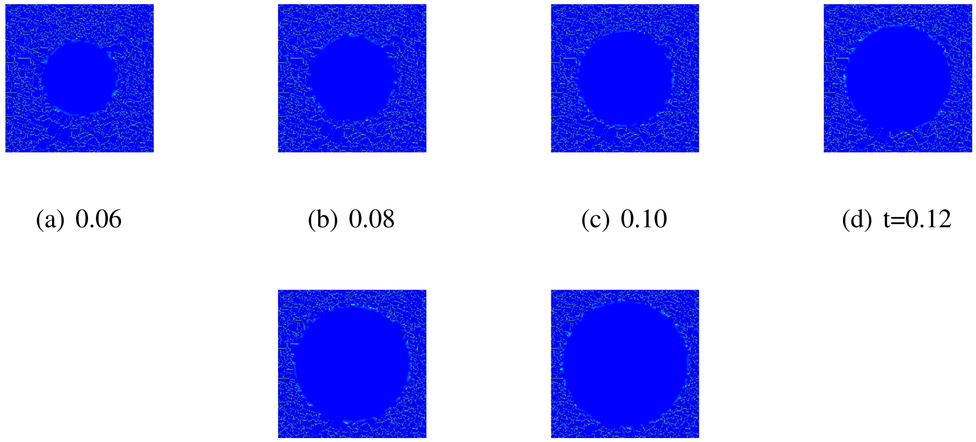

(a) 0.06 (b) 0.08 (c) 0.10 (d) t=0.12

(e) t=0.14 (f) t=0.16

Figure E.40: Solid binder contours of $\eta = 0.95$ heterogeneous material under C_2 loading conditions from $t = 0.06 - 0.16\mu s$.

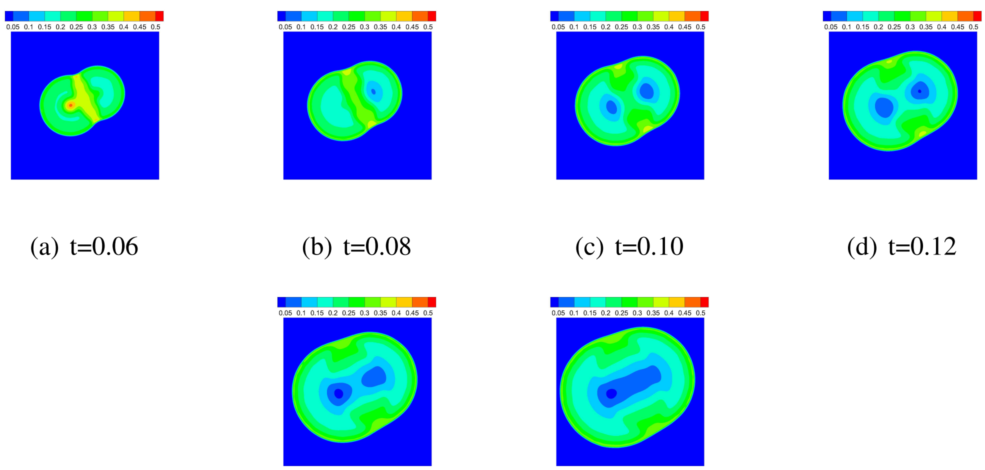

(a) t=0.06 (b) t=0.08 (c) t=0.10 (d) t=0.12

(e) t=0.14 (f) t=0.16

Figure E.41: Pressure contours of $\eta = 0.95$ heterogeneous material under B_Y loading conditions from $t = 0.06 - 0.16\mu s$.

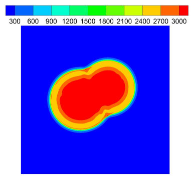

(a) t=0.06

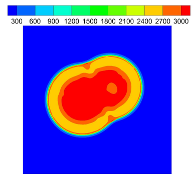

(b) t=0.08

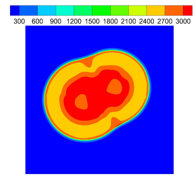

(c) t=0.10

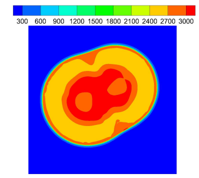

(d) t=0.12

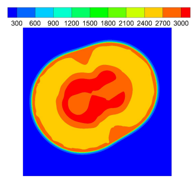

(e) t=0.14

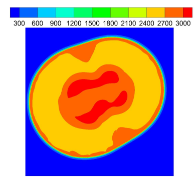

(f) t=0.16

Figure E.42: Temperature contours of $\eta = 0.95$ heterogeneous material under B_Y loading conditions from $t = 0.06 - 0.16\mu s$.

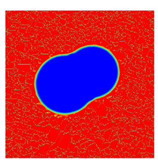

(a) t=0.06

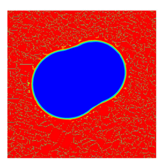

(b) t=0.08

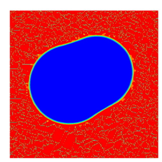

(c) t=0.10

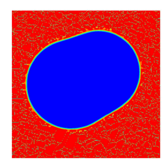

(d) t=0.12

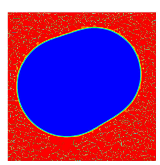

(e) 0.14

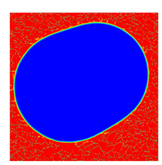

(f) 0.16

Figure E.43: HMX fraction contours of $\eta = 0.95$ heterogeneous material under B_Y loading conditions from $t = 0.06 - 0.16\mu s$.

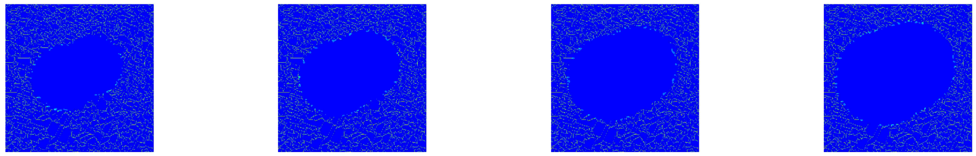

(a) 0.06 (b) 0.08 (c) 0.10 (d) t=0.12

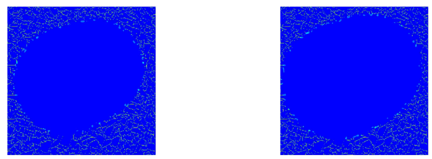

(e) t=0.14 (f) t=0.16

Figure E.44: Solid binder contours of $\eta = 0.95$ heterogeneous material under B_Y loading conditions from $t = 0.06 - 0.16\mu s$.

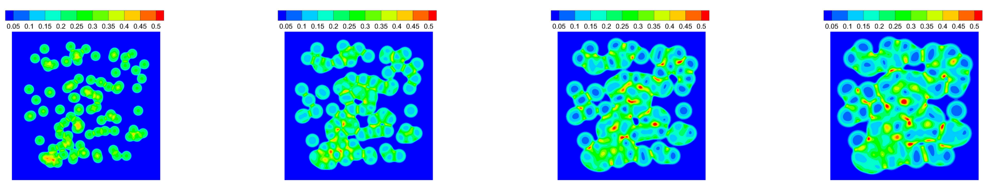

(a) t=0.01 (b) t=0.02 (c) t=0.03 (d) t=0.04

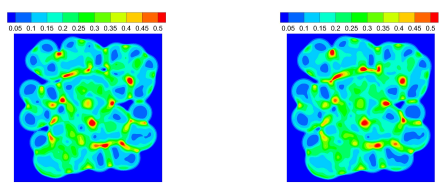

(e) t=0.05 (f) t=0.06

Figure E.45: Pressure contours of $\eta = 0.95$ heterogeneous material under B_Y loading conditions from $t = 0.06 - 0.16\mu s$.

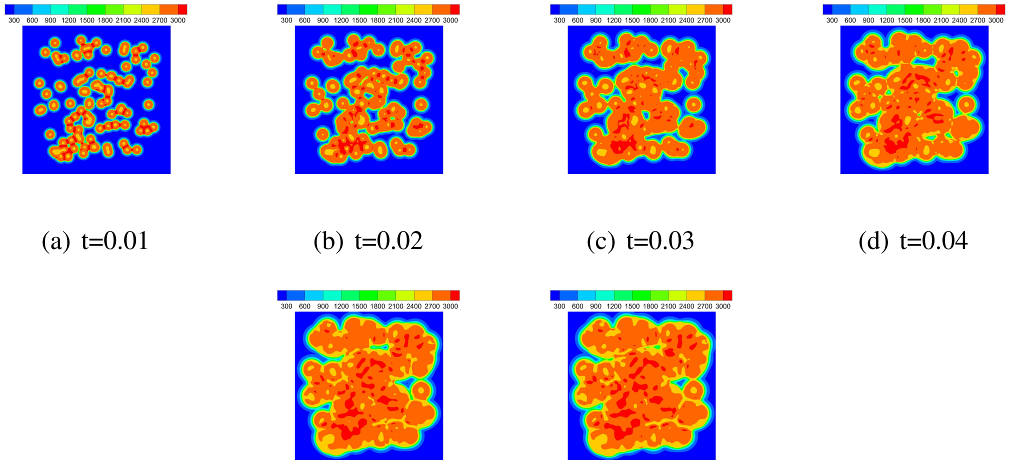

(a) t=0.01 (b) t=0.02 (c) t=0.03 (d) t=0.04

(e) t=0.05 (f) t=0.06

Figure E.46: Temperature contours of $\eta = 0.95$ heterogeneous material under B_Y loading conditions from $t = 0.06 - 0.16\mu s$.

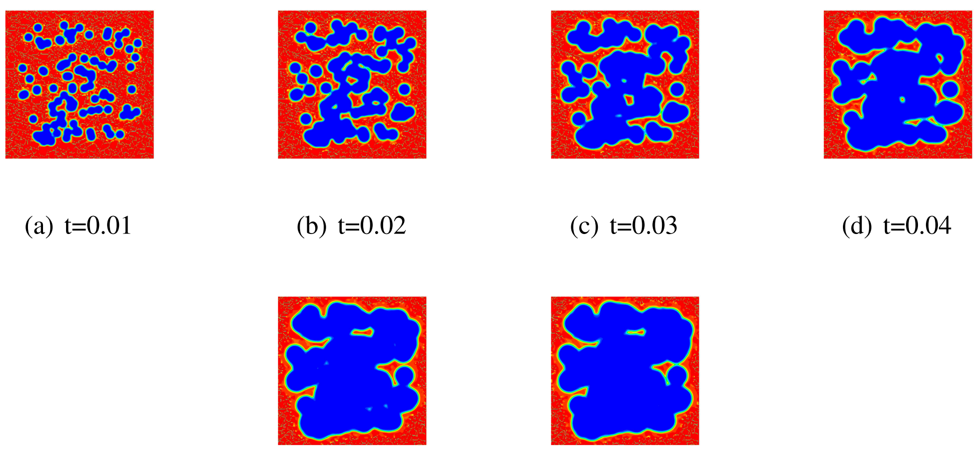

(a) t=0.01 (b) t=0.02 (c) t=0.03 (d) t=0.04

(e) t=0.05 (f) t=0.06

Figure E.47: HMX contours of $\eta = 0.95$ heterogeneous material under B_Y loading conditions from $t = 0.06 - 0.16\mu s$.

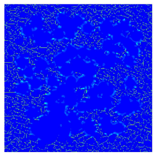

(a) t=0.01

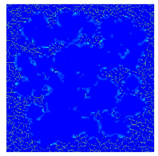

(b) t=0.02

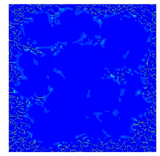

(c) t=0.03

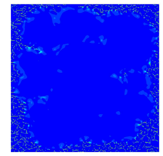

(d) t=0.04

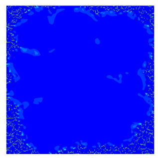

(e) t=0.05

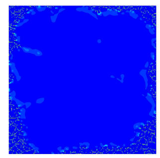

(f) t=0.06

Figure E.48: Binder contours of $\eta = 0.95$ heterogeneous material under R_m loading conditions from $t = 0.06 - 0.16\mu s$.

APPENDIX F

First-Order Multiscaling Numerical Results

This Appendix presents numerical results for First-Order Multiscaling of shock loading of polymer bonded explosives. The results supplement Chapter 5. A uniform mesh, using 3-noded constant strain triangle elements, is considered with a mesh density of $2000 ELM/cm$. A constant time step of $\Delta t = 1e-5 \mu s$ for a duration of $t = 0.16 \mu s$. Computationally, the solution procedure for all results used 8 computational nodes with 16 cores each for a total number of 128 processes.

F.1 Initial Conditions

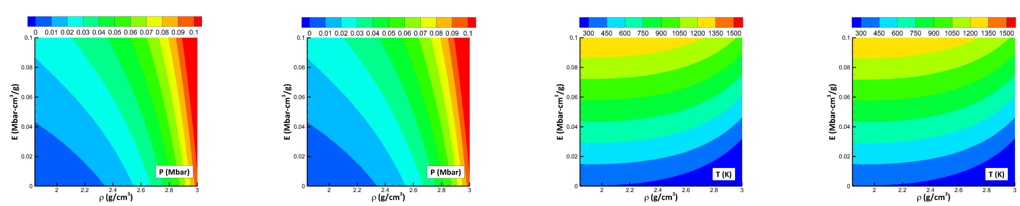

(a) Pressure, $\phi = 50$ (b) Pressure, $\phi = 1$ (c) Temperature $\phi = 50$ (d) Temperature $\phi = 1$

Figure F.1: Initial C_1 shock loading for $\eta = 0.75$ at various levels of coarseness.

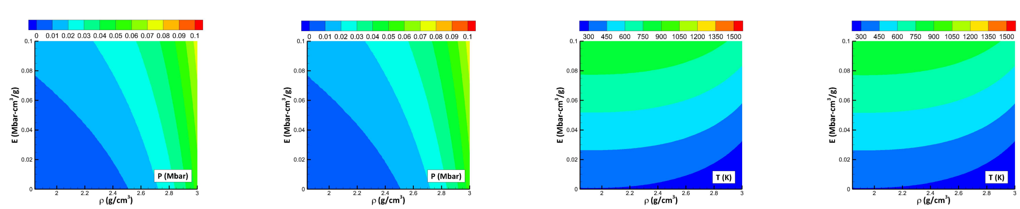

(a) Pressure, $\phi = 50$ (b) Pressure, $\phi = 1$ (c) Temperature $\phi = 50$ (d) Temperature $\phi = 1$

Figure F.2: Initial C_2 shock loading for $\eta = 0.75$ at various levels of coarseness.

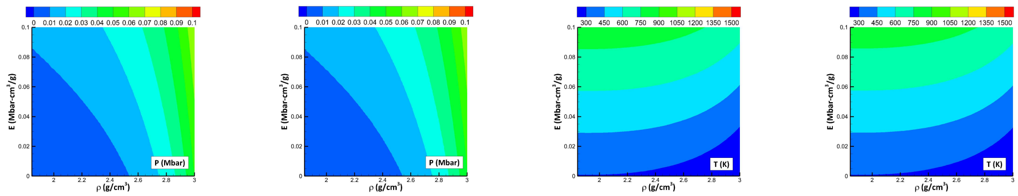

(a) Pressure, $\phi = 50$ (b) Pressure, $\phi = 1$ (c) Temperature $\phi = 50$ (d) Temperature $\phi = 1$

Figure F.3: Initial B_y shock loading for $\eta = 0.75$ at various levels of coarseness.

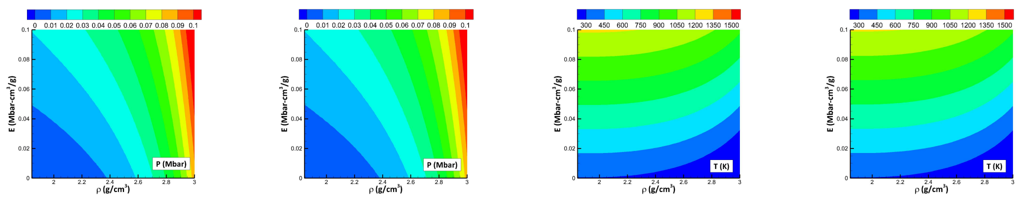

(a) Pressure, $\phi = 50$ (b) Pressure, $\phi = 1$ (c) Temperature $\phi = 50$ (d) Temperature $\phi = 1$

Figure F.4: Initial R_m shock loading for $\eta = 0.75$ at various levels of coarseness.

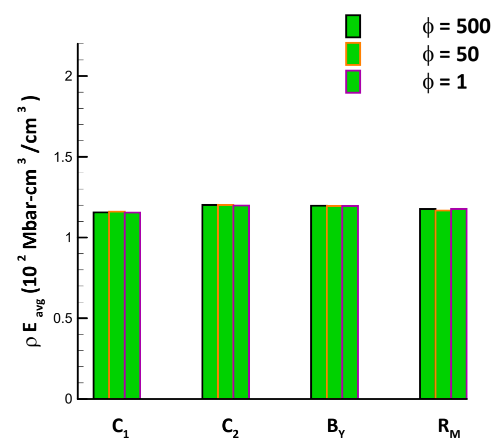

Figure F.5: Energy per unit volume for all loading conditions for $\eta = 0.75$ material system, with varying coarseness

Loading Condition	ρ (g/cm^3)	E $(Mbar-cm^3/g)$	$10^2 \frac{V_{hot}}{V_{total}}$	ρE_{avg} $(Mbar)$	P_{avg} (GPa)	T_{avg} (K)
$\boldsymbol{\eta = 0.75}$ $\boldsymbol{\phi = 50}$						
C_1	2.747	0.0336	12.56	0.0116	5.02	501.31
C_2	2.908	0.0585	7.06	0.0120	5.03	501.25
B_y	2.930	0.0645	6.34	0.0119	5.02	502.22
R_m	2.782	0.0381	10.95	0.0117	5.02	500.869
$\boldsymbol{\eta = 0.75}$ $\boldsymbol{\phi = 1}$						
C_1	2.745	0.0335	12.56	0.0115	5.01	500.63
C_2	2.907	0.0584	7.06	0.0119	5.02	501.1
B_y	2.935	0.0644	6.34	0.0119	4.99	499.64
R_m	2.784	0.0384	10.95	0.0118	5.03	502.83

Table F.1: Summary of initial conditions for $\eta = 0.75$ material system, with varying coarseness

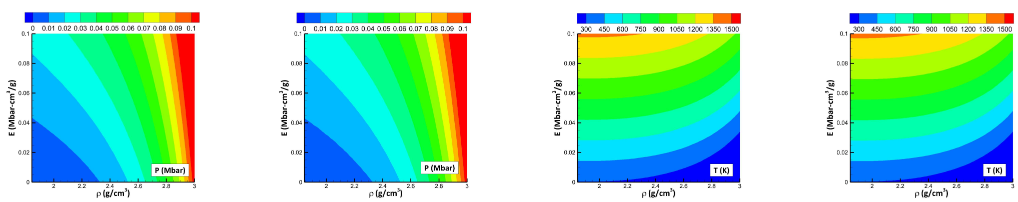

(a) Pressure, $\phi = 50$ (b) Pressure, $\phi = 1$ (c) Temperature $\phi = 50$ (d) Temperature $\phi = 1$

Figure F.6: Initial C_1 shock loading for $\eta = 0.85$ at various levels of coarseness.

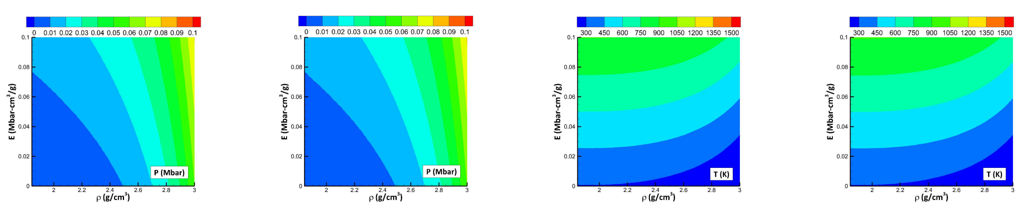

(a) Pressure, $\phi = 50$ (b) Pressure, $\phi = 1$ (c) Temperature $\phi = 50$ (d) Temperature $\phi = 1$

Figure F.7: Initial C_2 shock loading for $\eta = 0.85$ at various levels of coarseness.

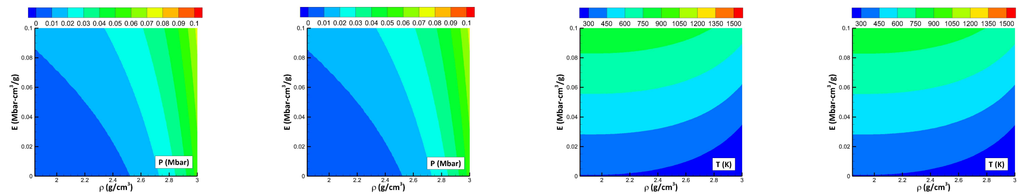

(a) Pressure, $\phi = 50$ (b) Pressure, $\phi = 1$ (c) Temperature $\phi = 50$ (d) Temperature $\phi = 1$

Figure F.8: Initial B_y shock loading for $\eta = 0.85$ at various levels of coarseness.

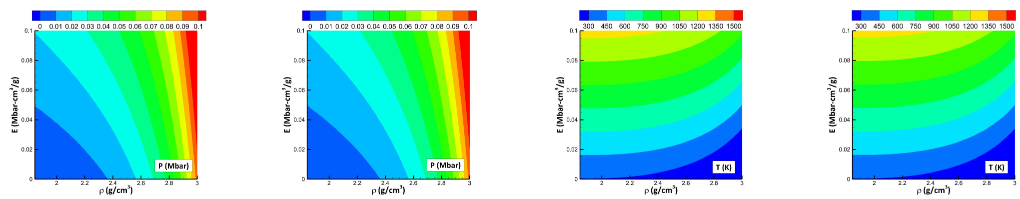

(a) Pressure, $\phi = 50$ (b) Pressure, $\phi = 1$ (c) Temperature $\phi = 50$ (d) Temperature $\phi = 1$

Figure F.9: Initial R_m shock loading for $\eta = 0.85$ at various levels of coarseness.

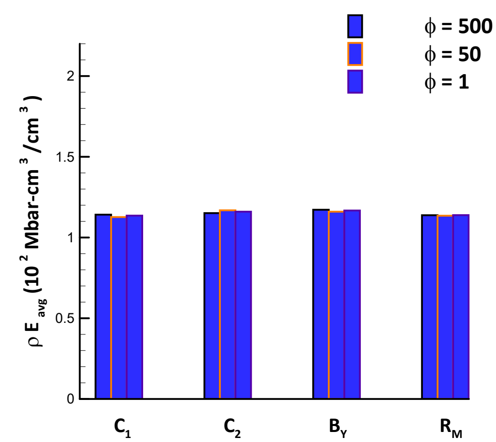

Figure F.10: Energy per unit volume for all loading conditions for $\eta = 0.85$ material system, with varying coarseness

Loading Condition	ρ (g/cm^3)	E $(Mbar-cm^3/g)$	$10^2 \frac{V_{hot}}{V_{total}}$	ρE_{avg} $(Mbar)$	P_{avg} (GPa)	T_{avg} (K)
$\boldsymbol{\eta = 0.85}$ $\boldsymbol{\phi = 50}$						
C_1	2.728	0.0329	12.56	0.0113	5.03	501.66
C_2	2.889	0.0573	7.06	0.0117	5.05	501.53
B_y	2.913	0.0639	6.34	0.0116	5.02	500.79
R_m	2.764	0.0373	10.95	0.0114	5.04	501.12
$\boldsymbol{\eta = 0.85}$ $\boldsymbol{\phi = 1}$						
C_1	2.735	0.0331	12.56	0.0113	5.15	500.16
C_2	2.886	0.0569	7.06	0.0116	5.01	500.74
B_y	2.914	0.0633	6.34	0.0116	5.00	502.19
R_m	2.765	0.0374	10.95	0.0113	5.04	501.62

Table F.2: Summary of initial conditions for $\eta = 0.85$ material system, with varying coarseness

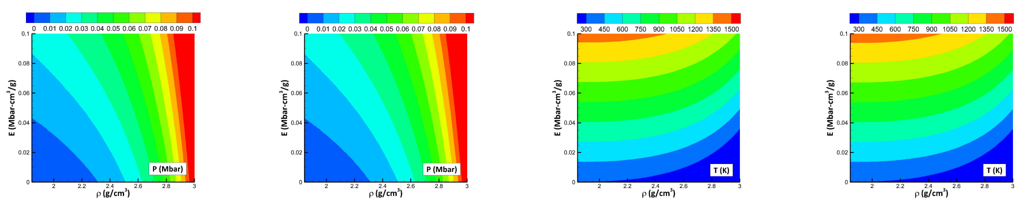

(a) Pressure, $\phi = 50$ (b) Pressure, $\phi = 1$ (c) Temperature $\phi = 50$ (d) Temperature $\phi = 1$

Figure F.11: Initial C_1 shock loading for $\eta = 0.95$ at various levels of coarseness.

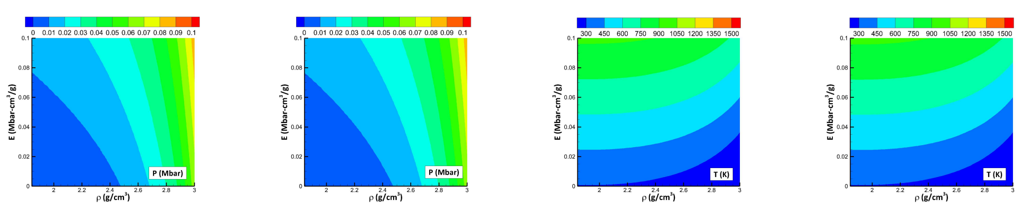

(a) Pressure, $\phi = 50$ (b) Pressure, $\phi = 1$ (c) Temperature $\phi = 50$ (d) Temperature $\phi = 1$

Figure F.12: Initial C_2 shock loading for $\eta = 0.95$ at various levels of coarseness.

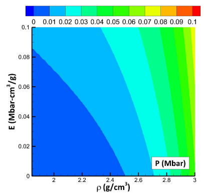

(a) Pressure, $\phi = 50$

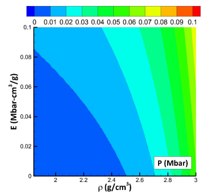

(b) Pressure, $\phi = 1$

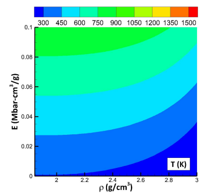

(c) Temperature $\phi = 50$

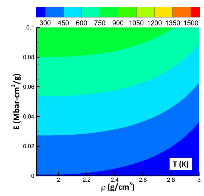

(d) Temperature $\phi = 1$

Figure F.13: Initial B_y shock loading for $\eta = 0.95$ at various levels of coarseness.

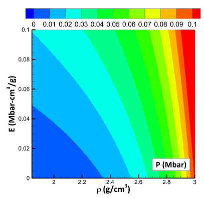

(a) Pressure, $\phi = 50$

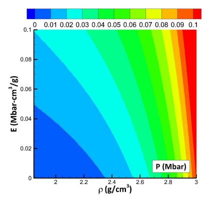

(b) Pressure, $\phi = 1$

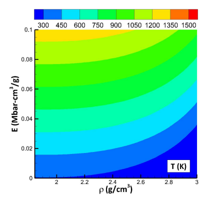

(c) Temperature $\phi = 50$

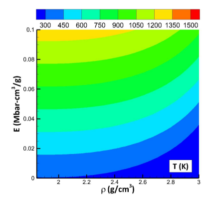

(d) Temperature $\phi = 1$

Figure F.14: Initial R_m shock loading for $\eta = 0.95$ at various levels of coarseness.

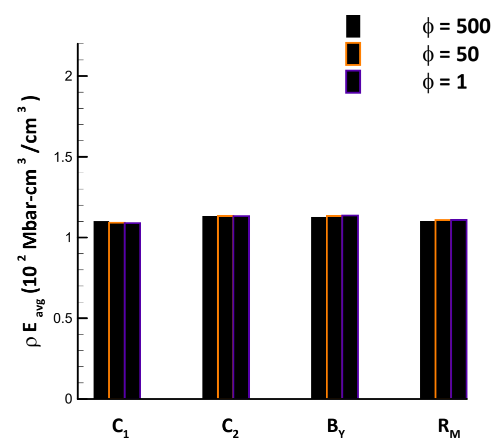

Figure F.15: Energy per unit volume for all loading conditions for $\eta = 0.95$ material system, with varying coarseness

Loading Condition	ρ (g/cm^3)	E $(Mbar-cm^3/g)$	$10^2\frac{V_{hot}}{V_{total}}$	ρE_{avg} $(Mbar)$	P_{avg} (GPa)	T_{avg} (K)
$\boldsymbol{\eta = 0.95}$ $\boldsymbol{\phi = 50}$						
C_1	2.710	0.0321	12.56	0.0109	5.04	501.56
C_2	2.870	0.0560	7.06	0.0113	5.05	501.80
B_y	2.898	0.0618	6.34	0.0113	5.03	500.71
R_m	2.748	0.0366	10.95	0.0111	5.05	501.91
$\boldsymbol{\eta = 0.95}$ $\boldsymbol{\phi = 1}$						
C_1	2.708	0.0320	12.56	0.0108	5.00	501.49
C_2	2.869	0.0558	7.06	0.0113	5.03	500.90
B_y	2.898	0.0620	6.34	0.0114	5.02	501.84
R_m	2.747	0.0366	10.95	0.0111	5.03	503.22

Table F.3: Summary of initial conditions for $\eta = 0.75$ material system, with varying coarseness

BIBLIOGRAPHY

[1] P. W. Cooper, *Explosives engineering*. Vch Pub, 1996.

[2] W. Fickett and W. C. Davis, "Detonation. berkeley," 1979.

[3] M. Gogulya, M. Makhov, A. Y. Dolgoborodov, M. Brazhnikov, V. Arkhipov, and V. Shchetinin, "Mechanical sensitivity and detonation parameters of aluminized explosives," *Combustion, Explosion and Shock Waves*, vol. 40, no. 4, pp. 445–457, 2004.

[4] H. Moulard, "Particular aspect of the explosive particle size effect on shock sensitivity of cast pbx formulations," in *Ninth Symposium (International) on Detonation*, pp. 113291–7, 1989.

[5] M. Gogulya, A. Y. Dolgoborodov, M. Brazhnikov, and G. Baudin, "Detonation waves in hmx/al mixtures (pressure and temperature measurements)," in *Proc. of the 11th Symp.(Int.) on Detonation*, pp. 979–988, 1998.

[6] M. Makhov, M. Gogulya, A. Y. Dolgoborodov, M. Brazhnikov, V. Arkhipov, and V. Pepekin, "Acceleration ability and heat of explosive decomposition of aluminized explosives," *Combustion, Explosion and Shock Waves*, vol. 40, no. 4, pp. 458–466, 2004.

[7] Z.-P. Duan, L.-J. Wen, Y. Liu, Z.-C. Ou, F.-L. Huang, and Z.-Y. Zhang, "A pore collapse model for hot-spot ignition in shocked multi-component explosives," *International Journal of Nonlinear Sciences and Numerical Simulation*, vol. 11, no. 12, pp. 19–23, 2010.

[8] S. Wallin, A. Pettersson, H. Östmark, and A. Hobro, "Laser-based standoff detection of explosives: a critical review," *Analytical and bioanalytical chemistry*, vol. 395, no. 2, pp. 259–274, 2009.

[9] M. A. Cook, *The science of high explosives*, vol. 139. RE Krieger Pub. Co., 1958.

[10] J. Akhavan, *The chemistry of explosives*. Royal Society of Chemistry, 2011.

[11] P. Balachandran, *Fundamentals of compressible fluid dynamics*. PHI Learning Pvt. Ltd., 2006.

[12] W. C. Davis, "High explosives: the interaction of chemistry and mechanics," *Los Alamos Science*, vol. 2, no. 1, pp. 48–75, 1981.

[13] A. Campbell, W. Davis, and J. Travis, "Shock initiation of detonation in liquid explosives," *The Physics of Fluids*, vol. 4, no. 4, pp. 498–510, 1961.

[14] S. Sheffield, R. Engelke, and R. Alcon, "Ninth symposium (international) on detonation," *Portland, Oregon, August*, 1989.

[15] F. P. Bowden and A. D. Yoffe, *Initiation and growth of explosion in liquids and solids*. CUP Archive, 1952.

[16] J. E. Field, "Hot spot ignition mechanisms for explosives," *Accounts of chemical Research*, vol. 25, no. 11, pp. 489–496, 1992.

[17] B. Khasainov, B. Ermolaev, H.-N. Presles, and P. Vidal, "On the effect of grain size on shock sensitivity of heterogeneous high explosives," *Shock Waves*, vol. 7, no. 2, pp. 89–105, 1997.

[18] R. Gustavsen, S. Sheffield, R. Alcon, and L. Hill, "Shock initiation of new and aged pbx 9501 measured with embedded electromagnetic particle velocity gauges," *LANL Report: LA-13634-MS*, 1999.

[19] S. Rybanin and Y. M. Mikhailov, "The number defining the realization of the hot spot mechanism on detonation of heterogeneous explosives," in *Doklady Physical Chemistry*, vol. 409, pp. 214–217, Springer, 2006.

[20] C. L. Mader, "Shock and hot spot initiation of homogeneous explosives," *The Physics of Fluids*, vol. 6, no. 3, pp. 375–381, 1963.

[21] D. Bradley, "hot spots and gasoline engine knock," *Journal of the Chemical Society, Faraday Transactions*, vol. 92, no. 16, pp. 2959–2964, 1996.

[22] M. Braithwaite, P. Lynch, I. Parker, A. Jones, and S. Wilson, "Compressional heating of isolated gas bubbles in reactive media," *Mathematical Engineering in Industry*, vol. 7, no. 3, pp. 361–387, 1999.

[23] D. M. Dattelbaum, S. A. Sheffield, and R. L. Gustavsen, "The shock-to-detonation transition in explosives-an overview,"

[24] J. Ramsay and A. Popolato, "Analysis of shock wave and initiation data for solid explosives," tech. rep., Los Alamos Scientific Lab., Univ. of California, N. Mex., 1965.

[25] W. E. Johnson and C. E. Anderson, "History and application of hydrocodes in hypervelocity impact," *International Journal of Impact Engineering*, vol. 5, no. 1-4, pp. 423–439, 1987.

[26] C. E. Anderson, "An overview of the theory of hydrocodes," *International journal of impact engineering*, vol. 5, no. 1-4, pp. 33–59, 1987.

[27] J. A. Zukas, T. Nicholas, H. F. Swift, L. B. Greszczuk, D. R. Curran, and L. Malvern, "Impact dynamics," *Journal of Applied Mechanics*, vol. 50, p. 702, 1983.

[28] R. L. Bowers and J. R. Wilson, "Numerical modeling in applied physics and astrophysics," *Boston: Jones and Bartlett, c1991.*, vol. 1, 1991.

[29] J. M. McGlaun, S. Thompson, and M. Elrick, "Cth: a three-dimensional shock wave physics code," *International Journal of Impact Engineering*, vol. 10, no. 1-4, pp. 351–360, 1990.

[30] J. O. Hallquist, "User's manual for dyna2d: An explicit two-dimensional hydrodynamic finite element code with interactive rezoning and graphical display," tech. rep., Lawrence Livermore National Lab., CA (USA), 1988.

[31] J. O. Hallquist, "Ls-dyna3d theoretical manual," *Livermore software technology corporation*, 1993.

[32] G. Johnson, R. Stryk, D. Pratt, and J. Schonhardt, "User instructions for the 1995 version of the epic code, alliant techsystems," *Inc, Brooklyn, Park, MN (October 1992)*, 1994.

[33] L. Taylor and D. Flanagan, "Pronto 2d: A two-dimensional transient solid dynamics program," tech. rep., Sandia National Labs., Albuquerque, NM (USA), 1987.

[34] L. Taylor and D. Flanagan, "Pronto 3d: A three-dimensional transient solid dynamics program," tech. rep., Sandia National Labs., Albuquerque, NM (USA), 1989.

[35] D. J. Benson, "Computational methods in lagrangian and eulerian hydrocodes," *Computer methods in Applied mechanics and Engineering*, vol. 99, no. 2-3, pp. 235–394, 1992.

[36] C. Hirt, A. A. Amsden, and J. Cook, "An arbitrary lagrangian-eulerian computing method for all flow speeds," *Journal of computational physics*, vol. 14, no. 3, pp. 227–253, 1974.

[37] D. L. Chapman, "Vi. on the rate of explosion in gases," *The London, Edinburgh, and Dublin Philosophical Magazine and Journal of Science*, vol. 47, no. 284, pp. 90–104, 1899.

[38] É. Jouguet, *Mécanique des explosifs*, vol. 10. Mame, 1917.

[39] A. Kapila, J. B. Bdzil, and D. S. Stewart, "On the structure and accuracy of programmed burn," *Combustion Theory and Modelling*, vol. 10, no. 2, pp. 289–321, 2006.

[40] Y. B. Zeldovich, "On the theory of the propagation of detonation in gaseous systems," 1950.

[41] J. Von Neuman, "Theory of detonation waves," tech. rep., DTIC Document, 1942.

[42] W. Döring, "On detonation processes in gases," *Ann. Phys*, vol. 43, no. 421-436, p. 9, 1943.

[43] C. Handley, M. Elert, M. D. Furnish, R. Chau, N. Holmes, and J. Nguyen, "The crest reactive burn model," in *AIP Conference Proceedings*, vol. 955, pp. 373–376, AIP, 2007.

[44] M. S. Shaw and R. Menikoff, "A reactive burn model for shock initiation in a pbx: Scaling and separability based on the hot spot concept," in *Fourteenth Symposium (International) on Detonation*, vol. 2, 2010.

[45] R. Menikoff and M. S. Shaw, "Reactive burn models and ignition & growth concept," in *EPJ Web of Conferences*, vol. 10, p. 00003, EDP Sciences, 2010.

[46] E. L. Lee and C. M. Tarver, "Phenomenological model of shock initiation in heterogeneous explosives," *The Physics of Fluids*, vol. 23, no. 12, pp. 2362–2372, 1980.

[47] B. Dobratz and P. Crawford, "Lln l explosives handbook," *UCRL-52997, Lawrence Livermore National Laboratory, CA*, 1985.

[48] T. R. Gibbs, *LASL explosive property data*, vol. 4. Univ of California Press, 1980.

[49] C. Addison and N. Logan, "The chemistry of dinitrogen pentoxide," in *Devel. Inorg. Nitrogen Chem.*, vol. 2, pp. 27–29, 1973.

[50] A. Elbeih, S. Zeman, M. Jungová, and P. Vávra, "Attractive nitramines and related pbxs," *Propellants, Explosives, Pyrotechnics*, vol. 38, no. 3, pp. 379–385, 2013.

[51] A. Provatas, "Formulation and performance studies of polymer bonded explosives (pbx) containing energetic binder systems. part i," 2003.

[52] A. Lundberg, "High explosives in stockpile surveillance indicate constancy," *Science and Technology Review*, 1996.

[53] D. Williamson, C. Siviour, W. Proud, S. Palmer, R. Govier, K. Ellis, P. Blackwell, and C. Leppard, "Temperature–time response of a polymer bonded explosive in compression (edc37)," *Journal of Physics D: Applied Physics*, vol. 41, no. 8, p. 085404, 2008.

[54] A. Gash, "High-explosive components using advanced manufacturing methods,"

[55] P. Peterson, M. Fletcher, and E. Roemer, "Influence of pressing intensity on the microstructure of pbx 9501," *Energetic Materials*, vol. 21, no. 4, pp. 247–260, 2003.

[56] C. Skidmore, D. Phillips, P. Howe, J. Mang, and J. Romero, "The evolution of microstructural changes in pressed hmx explosives," tech. rep., Los Alamos National Lab., NM (United States), 1998.

[57] C. B. Skidmore, D. S. Phillips, and N. B. Crane, "Microscopical examination of plastic-bonded explosives," tech. rep., Los Alamos National Lab., NM (United States), 1997.

[58] J. M. McAfee and R. Nelson, "Explosive morphology from fractal analysis of micrographs," tech. rep., Los Alamos National Lab., NM (United States), 1998.

[59] J. E. Field, "Hot spot ignition mechanisms for explosives," *Accounts of chemical Research*, vol. 25, no. 11, pp. 489–496, 1992.

[60] J. Clarke, S. Karni, J. Quirk, P. Roe, L. Simmonds, and E. Toro, "Numerical computation of two-dimensional unsteady detonation waves in high energy solids," *Journal of Computational Physics*, vol. 106, no. 2, pp. 215–233, 1993.

[61] R. J. LeVeque and H. C. Yee, "A study of numerical methods for hyperbolic conservation laws with stiff source terms," *Journal of computational physics*, vol. 86, no. 1, pp. 187–210, 1990.

[62] E. F. Byrd, G. E. Scuseria, and C. F. Chabalowski, "An ab initio study of solid nitromethane, hmx, rdx, and cl20: Successes and failures of dft," *The Journal of Physical Chemistry B*, vol. 108, no. 35, pp. 13100–13106, 2004.

[63] M. R. Manaa, L. E. Fried, C. F. Melius, M. Elstner, and T. Frauenheim, "Decomposition of hmx at extreme conditions: A molecular dynamics simulation," *The Journal of Physical Chemistry A*, vol. 106, no. 39, pp. 9024–9029, 2002.

[64] E. Bringa, J. Cazamias, P. Erhart, J. Stölken, N. Tanushev, B. Wirth, R. Rudd, and M. Caturla, "Atomistic shock hugoniot simulation of single-crystal copper," *Journal of Applied Physics*, vol. 96, no. 7, pp. 3793–3799, 2004.

[65] A. Strachan, E. M. Kober, A. C. van Duin, J. Oxgaard, and W. A. Goddard III, "Thermal decomposition of rdx from reactive molecular dynamics," *The Journal of chemical physics*, vol. 122, no. 5, p. 054502, 2005.

[66] T. D. Sewell, "Atomistic studies of fundamental properties and processes in energetic materials: relevance to mesoscale initiation phenomena," *Central European Journal of Energetic Materials*, vol. 3, no. 1-2, pp. 19–38, 2006.

[67] J.-B. Maillet, M. Mareschal, L. Soulard, R. Ravelo, P. S. Lomdahl, T. C. Germann, and B. L. Holian, "Uniaxial hugoniostat: A method for atomistic simulations of shocked materials," *Physical Review E*, vol. 63, no. 1, p. 016121, 2000.

[68] R. Ravelo, B. Holian, T. Germann, and P. Lomdahl, "Constant-stress hugoniostat method for following the dynamical evolution of shocked matter," *Physical Review B*, vol. 70, no. 1, p. 014103, 2004.

[69] E. J. Reed, L. E. Fried, and J. Joannopoulos, "A method for tractable dynamical studies of single and double shock compression," *Physical review letters*, vol. 90, no. 23, p. 235503, 2003.

[70] J. Reaugh, *Multi-scale computer simulations to study the reaction zone of solid explosives*. United States. Department of Energy, 2006.

[71] S. Lee and V. Sundararaghavan, "Calibration of nanocrystal grain boundary model based on polycrystal plasticity using molecular dynamics simulations," *International Journal for Multiscale Computational Engineering*, vol. 8, no. 5, pp. 509–522, 2010.

[72] V. Sundararaghavan and A. Kumar, "Molecular dynamics simulations of compressive yielding in cross-linked epoxies in the context of argon theory," *International Journal of Plasticity*, vol. 47, pp. 111 – 125, 2013.

[73] A. Kumar, V. Sundararaghavan, and A. R. Browning, "Study of temperature dependence of thermal conductivity in cross-linked epoxies using molecular dynamics simulations with long range interactions," *Modelling and Simulation in Materials Science and Engineering*, vol. 22, no. 2, p. 025013, 2014.

[74] N. Fasanella and V. Sundararaghavan, "Atomistic modeling of thermomechanical properties of swnt/epoxy nanocomposites," *Modelling and Simulation in Materials Science and Engineering*, vol. 23, no. 6, p. 065003, 2015.

[75] N. A. Fasanella and V. Sundararaghavan, "Atomistic modeling of thermal conductivity of epoxy nanotube composites," *JOM*, vol. 68, pp. 1396–1410, May 2016.

[76] A. L. Nichols III and C. M. Tarver, "A statistical hot spot reactive flow model for shock initiation and detonation of solid high explosives," in *Twelfth International Symposium on Detonation, Office of Naval Research, San Diego, CA*, 2002.

[77] Y. Hamate, Y. Horie, M. D. Furnish, Y. M. Gupta, and J. W. Forbes, "A statistical approach on mechanistic modeling of high-explosive ignition," in *AIP Conference Proceedings*, vol. 706, pp. 335–338, AIP, 2004.

[78] S. Kim, A. Barua, Y. Horie, and M. Zhou, "Ignition probability of polymer-bonded explosives accounting for multiple sources of material stochasticity," *Journal of Applied Physics*, vol. 115, no. 17, p. 174902, 2014.

[79] D. Swift, R. Mulford, R. Winter, P. Taylor, D. Salisbury, E. Harris, and A. Aldermaston, "Mesoscale modelling of reaction in hmx-based explosives," in *Twelfth International Detonation Symposium, volume ONR*, pp. 333–05, 2002.

[80] A. Barua, Y. Horie, and M. Zhou, "Microstructural level response of hmx–estane polymer-bonded explosive under effects of transient stress waves," in *Proc. R. Soc. A*, vol. 468, pp. 3725–3744, The Royal Society, 2012.

[81] E. Mas, B. Clements, and D. George, "Direct numerical simulations of pbx 9501," in *AIP Conference Proceedings*, American Institute of PhysicsAIP, 2004.

[82] B. Clements, E. Mas, M. D. Furnish, N. N. Thadhani, and Y. Horie, "Modeling high explosives with the method of cells and mori-tanaka effective medium theories," in *AIP Conference Proceedings*, vol. 620, pp. 427–430, AIP, 2002.

[83] K. Kline, Y. Horie, J. Dick, W. Wang, M. D. Furnish, N. N. Thadhani, and Y. Horie, "Impact response of pbx 9501 below 2 gpa," in *AIP Conference Proceedings*, vol. 620, pp. 411–414, AIP, 2002.

[84] S. Bardenhagen, J. Brackbill, and D. Sulsky, "Shear deformation in granular material," in *Eleventh International Detonation Symposium, volume ONR*, pp. 33300–5, Citeseer, 1998.

[85] S. Bardenhagen, K. Roessig, O. Byutner, J. Guilkey, D. Bedrov, and G. Smith, "Direct numerical simulation of weak shocks in granular material," in *Twelfth International Detonation Symposium, volume ONR*, pp. 333–05, 2002.

[86] R. Menikoff, E. Kober, M. D. Furnish, L. C. Chhabildas, and R. S. Hixson, "Compaction waves in granular hmx," in *AIP Conference Proceedings*, vol. 505, pp. 397–400, AIP, 2000.

[87] R. Menikoff, M. D. Furnish, N. N. Thadhani, and Y. Horie, "Compaction wave profiles in granular hmx," in *AIP Conference Proceedings*, vol. 620, pp. 979–982, AIP, 2002.

[88] R. Panchadhar, K. A. Gonthier, M. Elert, M. D. Furnish, W. W. Anderson, W. G. Proud, and W. T. Butler, "Meso-scale heating predictions for weak impact of granular energetic solids," in *AIP Conference Proceedings*, vol. 1195, pp. 1377–1380, AIP, 2009.

[89] M. Baer, M. Kipp, and F. v. Swol, "Micromechanical modeling of heterogeneous energetic materials," tech. rep., Sandia National Labs., Albuquerque, NM (United States), 1998.

[90] M. R. Baer, M. D. Furnish, L. C. Chhabildas, and R. S. Hixson, "Computational modeling of heterogeneous reactive materials at the mesoscale," in *AIP Conference Proceedings*, vol. 505, pp. 27–34, AIP, 2000.

[91] A. Brundage, R. Wixom, A. Tappan, G. Long, M. Elert, M. D. Furnish, W. W. Anderson, W. G. Proud, and W. T. Butler, "Mesoscale simulations of shock initiation in energetic materials characterized by three-dimensional nanotomography," in *AIP Conference Proceedings*, vol. 1195, pp. 315–318, AIP, 2009.

[92] M. Baer and W. Trott, "Theoretical and experimental mesoscale studies of impact-loaded granular explosive and simulant materials," in *Twelfth International Detonation Symposium, volume ONR*, pp. 333–05, 2002.

[93] P. M. Howe, D. J. Benson, M. D. Furnish, Y. M. Gupta, and J. W. Forbes, "Progress in the development of a shock initiation model," in *AIP Conference Proceedings*, vol. 706, pp. 343–346, AIP, 2004.

[94] C. A. Handley, *Numerical modelling of two HMX-based plastic-bonded explosives at the mesoscale*. PhD thesis, University of St Andrews, 2011.

[95] E. B. Tadmor, M. Ortiz, and R. Phillips, "Quasicontinuum analysis of defects in solids," *Philosophical magazine A*, vol. 73, no. 6, pp. 1529–1563, 1996.

[96] J. M. Powers, "Review of multiscale modeling of detonation," *Journal of Propulsion and Power*, vol. 22, no. 6, pp. 1217–1229, 2006.

[97] E. Weinan, B. Engquist, and Y. Sun, "The heterogeneous multiscale methods with application to combustion," in *Turbulent Combustion Modeling*, pp. 439–459, Springer, 2011.

[98] V. Sundararaghavan and N. Zabaras, "Design of microstructure-sensitive properties in elasto-viscoplastic polycrystals using multi-scale homogenization," *International Journal of Plasticity*, vol. 22, no. 10, pp. 1799 – 1824, 2006.

[99] V. Sundararaghavan and N. Zabaras, "A multi-length scale sensitivity analysis for the control of texture-dependent properties in deformation processing," *International Journal of Plasticity*, vol. 24, no. 9, pp. 1581 – 1605, 2008.

[100] S. Lee and V. Sundararaghavan, "Multi-scale homogenization of moving interface problems with flux jumps: application to solidification," *Computational Mechanics*, vol. 44, pp. 297–307, Aug 2009.

[101] S. Lee and V. Sundararaghavan, "Multi-scale modeling of moving interface problems with flux and field jumps: Application to oxidative degradation of ceramic matrix composites," *International Journal for Numerical Methods in Engineering*, vol. 85, no. 6, pp. 784–804, 2011.

[102] S. M. Peiris and G. J. Piermarini, *Static compression of energetic materials*. Springer, 2008.

[103] P. C. Souers, S. Anderson, J. Mercer, E. McGuire, and P. Vitello, "Jwl++: a simple reactive flow code package for detonation," *Propellants, Explosives, Pyrotechnics*, vol. 25, no. 2, pp. 54–58, 2000.

[104] R. Menikoff and T. D. Sewell, "Constituent properties of hmx needed for mesoscale simulations," *Combustion theory and modelling*, vol. 6, no. 1, pp. 103–125, 2002.

[105] D. Bedrov, G. D. Smith, and T. D. Sewell, "Thermal conductivity of liquid octahydro-1, 3, 5, 7-tetranitro-1, 3, 5, 7-tetrazocine (hmx) from molecular dynamics simulations," *Chemical Physics Letters*, vol. 324, no. 1, pp. 64–68, 2000.

[106] R. Menikoff, "Detonation waves in pbx 9501," *Combustion Theory and Modelling*, vol. 10, no. 6, pp. 1003–1021, 2006.

[107] R. McGuire and C. Tarver, "Chemical-decomposition models for the thermal explosion of confined hmx, tatb, rdx, and tnt explosives," tech. rep., Lawrence Livermore National Lab., CA (USA), 1981.

[108] B. F. Henson, B. W. Asay, L. B. Smilowitz, P. M. Dickson, M. D. Furnish, N. N. Thadhani, and Y. Horie, "Ignition chemistry in hmx from thermal explosion to detonation," in *AIP Conference Proceedings*, vol. 620, pp. 1069–1072, AIP, 2002.

[109] C. M. Tarver and T. D. Tran, "Thermal decomposition models for hmx-based plastic bonded explosives," *Combustion and Flame*, vol. 137, no. 1, pp. 50–62, 2004.

[110] E. S. Oran and J. P. Boris, *Numerical simulation of reactive flow*. Cambridge University Press, 2005.

[111] W. H. Raymond and A. Garder, "Selective damping in a galerkin method for solving wave problems with variable grids," *Monthly weather review*, vol. 104, no. 12, pp. 1583–1590, 1976.

[112] A. N. Brooks and T. J. Hughes, "Streamline upwind/petrov-galerkin formulations for convection dominated flows with particular emphasis on the incompressible navier-stokes equations," *Computer methods in applied mechanics and engineering*, vol. 32, no. 1-3, pp. 199–259, 1982.

[113] J. Donea, "A taylor–galerkin method for convective transport problems," *International Journal for Numerical Methods in Engineering*, vol. 20, no. 1, pp. 101–119, 1984.

[114] A. Baker and J. Kim, "A taylor weak-statement algorithm for hyperbolic conservation laws," *International journal for numerical methods in fluids*, vol. 7, no. 5, pp. 489–520, 1987.

[115] R. Löhner, K. Morgan, and O. C. Zienkiewicz, "The solution of non-linear hyperbolic equation systems by the finite element method," *International Journal for Numerical Methods in Fluids*, vol. 4, no. 11, pp. 1043–1063, 1984.

[116] E. A. Thornton and R. Ramakrishnan, "Supercomputer implementation of finite element algorithms for high speed compressible flows," 1986.

[117] V. Nassehi and J. Bikangaga, "A mathematical model for the hydrodynamics and pollutants transport in long and narrow tidal rivers," *Applied mathematical modelling*, vol. 17, no. 8, pp. 415–422, 1993.

[118] M. Quecedo and M. Pastor, "A reappraisal of taylor–galerkin algorithm for drying–wetting areas in shallow water computations," *International journal for numerical methods in fluids*, vol. 38, no. 6, pp. 515–531, 2002.

[119] R. Löhner, K. Morgan, J. Peraire, and M. Vahdati, "Finite element flux-corrected transport (fem–fct) for the euler and navier–stokes equations," *International Journal for Numerical Methods in Fluids*, vol. 7, no. 10, pp. 1093–1109, 1987.

[120] A. V. Duran and V. Sundararaghavan, "Modeling the mechanics of hmx detonation using a taylor–galerkin scheme," *Theoretical and Applied Mechanics Letters*, vol. 6, no. 3, pp. 143–147, 2016.

[121] A. V. Duran and V. Sundararaghavan, "Finite element code development for modeling detonation of hmx composites," in *AIP Conference Proceedings*, vol. 1793, p. 080003, AIP Publishing, 2017.

[122] A. V. Duran and V. Sundararaghavan, "Modeling of shock wave propagation through energetic solid state composites using a taylor-galerkin scheme," in *57th AIAA/ASCE/AHS/ASC Structures, Structural Dynamics, and Materials Conference*, p. 1172, 2016.

[123] R. D. Cook, *Concepts and applications of finite element analysis: a treatment of the finite element method as used for the analysis of displacement, strain, and stress*. John Wiley & Sons, 1974.

[124] J. VonNeumann and R. D. Richtmyer, "A method for the numerical calculation of hydrodynamic shocks," *Journal of applied physics*, vol. 21, no. 3, pp. 232–237, 1950.

[125] B. Van Leer, "Towards the ultimate conservative difference scheme. iv. a new approach to numerical convection," *Journal of computational physics*, vol. 23, no. 3, pp. 276–299, 1977.

[126] S. Chakravarthy and S. Osher, "High resolution applications of the osher upwind scheme for the euler equations," in *6th Computational Fluid Dynamics Conference Danvers*, p. 1943, 1983.

[127] P. Roe, "Characteristic-based schemes for the euler equations," *Annual review of fluid mechanics*, vol. 18, no. 1, pp. 337–365, 1986.

[128] J. Donea and A. Huerta, *Finite element methods for flow problems*. John Wiley & Sons, 2003.

[129] M. Bull, X. Guo, and I. Liabotis, "Applications and user requirements for tier-0 systems," 2013.

[130] S. Balay, J. Brown, K. Buschelman, V. Eijkhout, W. Gropp, D. Kaushik, M. Knepley, L. C. McInnes, B. Smith, and H. Zhang, "Petsc users manual revision 3.3," *Computer Science Division, Argonne National Laboratory, Argonne, IL*, 2012.

[131] E. F. Toro, *Riemann solvers and numerical methods for fluid dynamics: a practical introduction*. Springer Science & Business Media, 2013.

[132] A. C. Berkenbosch, "Capturing detonation waves for the reactive euler equations," 1995.

[133] C. Tarver, J. Forbes, F. Garcia, P. Urtiew, M. D. Furnish, N. N. Thadhani, and Y. Horie, "Manganin gauge and reactive flow modeling study of the shock initiation of pbx 9501," in *AIP Conference Proceedings*, vol. 620, pp. 1043–1046, AIP, 2002.

[134] K. S. Vandersall, C. M. Tarver, F. Garcia, P. A. Urtiew, M. D. Furnish, M. Elert, T. P. Russell, and C. T. White, "Shock initiation experiments on pbx9501 explosive at 150 c for ignition and growth modeling," in *AIP Conference Proceedings*, vol. 845, pp. 1127–1130, AIP, 2006.

[135] V. Sundararaghavan and N. Zabaras, "A dynamic material library for the representation of single-phase polyhedral microstructures," *Acta Materialia*, vol. 52, no. 14, pp. 4111 – 4119, 2004.

[136] D. J. Heeger and J. R. Bergen, "Pyramid-based texture analysis/synthesis," in *Proceedings of the 22nd annual conference on Computer graphics and interactive techniques*, pp. 229–238, ACM, 1995.

[137] J. S. De Bonet, "Multiresolution sampling procedure for analysis and synthesis of texture images," in *Proceedings of the 24th annual conference on Computer graphics and interactive techniques*, pp. 361–368, ACM Press/Addison-Wesley Publishing Co., 1997.

[138] E. P. Simoncelli and J. Portilla, "Texture characterization via joint statistics of wavelet coefficient magnitudes," in *Image Processing, 1998. ICIP 98. Proceedings. 1998 International Conference on*, vol. 1, pp. 62–66, IEEE, 1998.

[139] S. Torquato, *Random heterogeneous materials: microstructure and macroscopic properties*, vol. 16. Springer Science & Business Media, 2013.

[140] E. Ising, "Beitrag zur theorie des ferromagnetismus," *Zeitschrift für Physik A Hadrons and Nuclei*, vol. 31, no. 1, pp. 253–258, 1925.

[141] C. E. Shannon, "A mathematical theory of communication," *ACM SIGMOBILE Mobile Computing and Communications Review*, vol. 5, no. 1, pp. 3–55, 2001.

[142] A. A. Efros and T. K. Leung, "Texture synthesis by non-parametric sampling," in *Computer Vision, 1999. The Proceedings of the Seventh IEEE International Conference on*, vol. 2, pp. 1033–1038, IEEE, 1999.

[143] K. Popat and R. W. Picard, "Novel cluster-based probability model for texture synthesis, classification, and compression," in *Visual Communications' 93*, pp. 756–768, International Society for Optics and Photonics, 1993.

[144] S. C. Zhu, Y. Wu, and D. Mumford, "Filters, random fields and maximum entropy (frame): Towards a unified theory for texture modeling," *International Journal of Computer Vision*, vol. 27, no. 2, pp. 107–126, 1998.

[145] R. Paget and I. D. Longstaff, "Texture synthesis via a noncausal nonparametric multiscale markov random field," *IEEE transactions on image processing*, vol. 7, no. 6, pp. 925–931, 1998.

[146] G. Mariethoz and S. Lefebvre, “Bridges between multiple-point geostatistics and texture synthesis: Review and guidelines for future research,” *Computers & Geosciences*, vol. 66, pp. 66–80, 2014.

[147] A. Kumar, L. Nguyen, M. DeGraef, and V. Sundararaghavan, “A markov random field approach for microstructure synthesis,” *Modelling and Simulation in Materials Science and Engineering*, vol. 24, no. 3, p. 035015, 2016.

[148] V. Kwatra, I. Essa, A. Bobick, and N. Kwatra, “Texture optimization for example-based synthesis,” *ACM Transactions on Graphics (ToG)*, vol. 24, no. 3, pp. 795–802, 2005.

[149] J. Kopf, C.-W. Fu, D. Cohen-Or, O. Deussen, D. Lischinski, and T.-T. Wong, “Solid texture synthesis from 2d exemplars,” in *ACM Transactions on Graphics (TOG)*, vol. 26, p. 2, ACM, 2007.

[150] V. Sundararaghavan, “Reconstruction of three-dimensional anisotropic microstructures from two-dimensional micrographs imaged on orthogonal planes,” *Integrating Materials and Manufacturing Innovation*, vol. 3, no. 1, p. 19, 2014.

[151] P. Acar and V. Sundararaghavan, “A markov random field approach for modeling spatio-temporal evolution of microstructures,” *Modelling and Simulation in Materials Science and Engineering*, vol. 24, no. 7, p. 075005, 2016.

[152] V. Sundararaghavan and N. Zabaras, “Classification and reconstruction of three-dimensional microstructures using support vector machines,” *Computational Materials Science*, vol. 32, no. 2, pp. 223–239, 2005.

[153] C. Yeong and S. Torquato, “Reconstructing random media. ii. three-dimensional media from two-dimensional cuts,” *Physical Review E*, vol. 58, no. 1, p. 224, 1998.

[154] C. Manwart, S. Torquato, and R. Hilfer, “Stochastic reconstruction of sandstones,” *Physical Review E*, vol. 62, no. 1, p. 893, 2000.

[155] J. Besag, “Spatial interaction and the statistical analysis of lattice systems,” *Journal of the Royal Statistical Society. Series B (Methodological)*, pp. 192–236, 1974.

[156] M. Grigoriu, “Nearest neighbor probabilistic model for aluminum polycrystals,” *Journal of engineering mechanics*, vol. 136, no. 7, pp. 821–829, 2010.

[157] S. Lefebvre and H. Hoppe, “Appearance-space texture synthesis,” *ACM Transactions on Graphics (TOG)*, vol. 25, no. 3, pp. 541–548, 2006.

[158] M. Ashikhmin, “Synthesizing natural textures,” in *Proceedings of the 2001 symposium on Interactive 3D graphics*, pp. 217–226, ACM, 2001.

[159] Q. Wu and Y. Yu, “Feature matching and deformation for texture synthesis,” *ACM Transactions on Graphics (TOG)*, vol. 23, no. 3, pp. 364–367, 2004.

[160] S. Zelinka and M. Garland, "Jump map-based interactive texture synthesis," *ACM Transactions on Graphics (TOG)*, vol. 23, no. 4, pp. 930–962, 2004.

[161] X. Tong, J. Zhang, L. Liu, X. Wang, B. Guo, and H.-Y. Shum, "Synthesis of bidirectional texture functions on arbitrary surfaces," in *ACM Transactions on Graphics (ToG)*, vol. 21, pp. 665–672, ACM, 2002.

[162] L.-Y. Wei, S. Lefebvre, V. Kwatra, and G. Turk, "State of the art in example-based texture synthesis," in *Eurographics 2009, State of the Art Report, EG-STAR*, pp. 93–117, Eurographics Association, 2009.

[163] N. S. Altman, "An introduction to kernel and nearest-neighbor nonparametric regression," *The American Statistician*, vol. 46, no. 3, pp. 175–185, 1992.

[164] N. Zabaras, V. Sundararaghavan, and S. Sankaran, "An information theoretic approach for obtaining property pdfs from macro specifications of microstructural uncertainty," *TMS letters*, vol. 3, no. 1, pp. 1 – 4, 2006.

[165] P. Acar and V. Sundararaghavan, "Uncertainty quantification of microstructural properties due to variability in measured pole figures," *Acta Materialia*, vol. 124, pp. 100 – 108, 2017.

[166] N. R. Barton, J. Knap, A. Arsenlis, R. Becker, R. D. Hornung, and D. R. Jefferson, "Embedded polycrystal plasticity and adaptive sampling," *International Journal of Plasticity*, vol. 24, no. 2, pp. 242–266, 2008.

[167] V. Sundararaghavan and N. Zabaras, "On the synergy between texture classification and deformation process sequence selection for the control of texture-dependent properties," *Acta Materialia*, vol. 53, no. 4, pp. 1015 – 1027, 2005.

[168] V. Sundararaghavan and N. Zabaras, "A statistical learning approach for the design of polycrystalline materials," *Statistical Analysis and Data Mining*, vol. 1, no. 5, pp. 306–321, 2009.

[169] V. Sundararaghavan and A. Kumar, "Probabilistic modeling of microstructure evolution using finite element representation of statistical correlation functions," *International Journal of Plasticity*, vol. 30, pp. 62 – 80, 2012.

[170] S. Sun and V. Sundararaghavan, "A probabilistic crystal plasticity model for modeling grain shape effects based on slip geometry," *Acta Materialia*, vol. 60, no. 13, pp. 5233 – 5244, 2012.

[171] V. Sundararaghavan, A. Kumar, and S. Sun, "Crystal plasticity simulations using nearest neighbor orientation correlation function," *Acta Materialia*, vol. 93, pp. 12 – 23, 2015.

[172] V. Sundararaghavan and N. Zabaras, "Linear analysis of textureproperty relationships using process-based representations of rodrigues space," *Acta Materialia*, vol. 55, no. 5, pp. 1573 – 1587, 2007.

[173] A. Duran, N. Fasanella, V. Sundararaghavan, and A. Waas, “Thermal buckling of composite plates with spatial varying fiber orientations,” *Composite Structures*, vol. 124, pp. 228 – 235, 2015.

[174] R. Liu, A. Kumar, Z. Chen, A. Agrawal, V. Sundararaghavan, and A. Choudhary, “A predictive machine learning approach for microstructure optimization and materials design,” *Scientific reports*, vol. 5, no. 11551, pp. 1 – 12, 2015.

[175] P. Acar and V. Sundararaghavan, “Utilization of a linear solver for multiscale design and optimization of microstructures,” *AIAA Journal*, vol. 54, no. 5, pp. 1751 – 1759, 2016.